Atomic Layer Deposition of CeO_x Nanoclusters on TiO_2

Ji Liu[a], Saeed Saedy[b], Rakshita Verma[b], J. Ruud van Ommen[b*], Michael Nolan[a,*]

[a] Tyndall National Institute, University College Cork, Lee Maltings, Dyke Parade, Cork, T12 R5CP, Ireland

[b] Product & Process Engineering, Department of Chemical Engineering, Delft University of Technology, Mekelweg 5, 2628 CD Delft, The Netherlands

Corresponding authors:

*E-mail: Michael.nolan@tyndall.ie, J.r.VanOmmen@tudelft.nl

Abstract

Titanium dioxide has a band-gap in the ultra violet region and there have been many efforts to shift light absorption to the visible region. In this regard, surface modification with metal oxide clusters has been used to promote band-gap reduction. CeO_x-modified TiO_2 materials have exhibited enhanced catalytic activity in water gas shift, but the deposition process used is not well-understood or suitable for powder materials. Atomic layer deposition (ALD) has been used for deposition of cerium oxide on TiO_2. The experimentally reported growth rates using typical Ce metal precursors such as β-diketonates and cyclopentadienyls are low, with reported growth rates of *ca.* 0.2-0.4 □/cycle. In this paper, we have performed density functional theory calculations to reveal the reaction mechanism of the metal precursor pulse together with experimental studies of ALD of CeO_x using two Ce precursors, $Ce(TMHD)_4$ and $Ce(MeCp)_3$. The nature and stability of hydroxyl groups on anatase and rutile TiO_2 surfaces are determined and used as starting substrates. Adsorption of the cerium precursors on the hydroxylated TiO_2 surfaces reduces the coverage of surface hydroxyls. Computed activation barriers for ligand elimination in $Ce(MeCp)_3$ indicate that ligand elimination is not possible on anatase (101) and rutile (100) surface, but it is possible on anatase (001) and rutile (110). The ligand elimination in $Ce(TMHD)_4$ is via breaking the Ce-O bond and hydrogen transfer from hydroxyl groups. For this precursor, the ligand elimination on the majority surface facets of anatase and rutile TiO_2 are endothermic and not favourable. It is difficult to deposit Ce atom onto hydroxylated TiO_2 surface using $Ce(TMHD)_4$ as precursor. Attempts for deposit cerium oxide on TiO_2 nanoparticles that expose the anatase (101) surface show at best a low deposition rate and this can be explained by the non-favorable ligand elimination reactions at this surface.

I. INTRODUCTION

Titanium dioxide (TiO_2) has attracted significant attention in many technologies, particularly in photocatalysis and solar energy conversion due to the push to move to renewable energies.[1-3] The main advantages of TiO_2 are its high abundance, low-cost and robustness under operating condition. Anatase and rutile are the two most widely studied polymorphs of TiO_2[4-6] and anatase is the most photocatalytically active phase. Early studies showed that bulk TiO_2 prefers the rutile structure, but the anatase structure is more stable for TiO_2 nanoparticles.[7, 8] Typically the mixed rutile-anatase phase P25 is used in studies of modified TiO_2.

Due to large band-gap of undoped TiO_2, which is *ca.* 3.0 - 3.2eV, in the UV range, cation and anion doping have been widely applied to achieve visible light adsorption and increase the photocatalytic efficiency.[9-11] Defects and impurities, such as the O-vacancy, play an important role in determining the reactivity of TiO_2. Alternatively, surface modification of TiO_2 with dispersed metal oxide nanoclusters has been developed to enhance the photocatalytic reactivity.[12-14] Platinum catalysts supported on ceria modified TiO_2 are highly active for the water-gas shift reaction and the loading of ceria can influence the activity. The improved chemical activity is associated with the presence of CeO_x clusters on TiO_2 surface.[15] Previous studies in our group and from experimental groups have indicated the potential for metal oxide modifiers to induce a bandgap reduction compared to bare TiO_2.[16-18] The presence of reduced Ce ions, namely Ce^{3+}, in supported CeO_x and low coordinated O sites in the nanocluster lead to red shift in light adsorption. Enhanced photocatalytic activity is found on nanostructured CeO_x/TiO_2 with nanobelt heterostructure and yolk-shell microsphere structure.[19-21]

The deposition of nanostructured CeO_x has been achieved using traditional approaches, such as approaches including calcination of organic precursors, precipitation and hydrothermal synthesis.[22, 23] However, these do not necessarily provide a high degree of control of deposition

and are also not ideal for deposition onto powder materials. To achieve the precise control of composition, loading and morphology of nanoclusters onto substrate, atomic layer deposition (ALD) can be used.[24] The advantages of ALD are self-limiting and saturated surface chemistry reactions with a high degree of control over deposition and loading.[25]

Choosing a stable metal precursor is still a significant challenge for the deposition of metal oxides. Basic criteria include stability and volatility, ease of handling, self-saturating growth characteristics, high growth rate, and reactivity with O-containing reactants. For cerium a range of organometallic precursors such as β-diketonates, alkoxides and cyclopentadienyls have been developed and used.[26-29] The reported growth rate using $Ce(THD)_4$ (thd = 2,2,6,6-tetramethyl-3,5-heptanedionate) is 0.32 □/cycle in a temperature range of 175 - 250 °C and the deposited films have impurities including hydrogen and carbon.[24] A growth rate of 1.9 □/cycle is found at growth temperatures of 165 - 285 °C using a heteroleptic cyclopentadienyl-amidinate precursor $Ce(iPeCp)_2$(N-iPr-amd).[30] However, the synthesis of heteroleptic cerium complex is rather difficult. The development of efficient and convenient CeO_x precursors is still required.

Understanding the reaction mechanism is useful and helpful for choosing a suitable precursor. In early work, the deposition of Al_2O_3 from trimethlyaluminum and H_2O was developed and studied both experimentally and theoretically.[31-35] Detailed density functional theory (DFT) studies have indicated that surface hydroxyl groups are produced after each cycle and their surface coverage affects the growth rate. Ligands are eliminated by proton transfer from surface OH groups and desorption. The oxidising reactant can be water or ozone, which has a higher activity for ligand elimination relative to H_2O. This mechanism involves precursor adsorption, proton transfer, and ligand elimination process, which has also been investigated in other metal oxide ALD processes such as TiO_2 and SiO_2.[36-41]

In this study, we have studied the adsorption and ligand elimination process for two cerium precursors Tris(methylcyclopentadienyl)cerium(III) ($Ce(MeCp)_3$) and Tetrakis(2,2,6,6-tetramethyl-3,5-heptanedionato)cerium(IV) ($Ce(TMHD)_4$) on TiO_2 using density functional theory, while ALD experiments are carried out with Tris(i-propylcyclopentadienyl)cerium(III), $Ce(^iPrCp)_3$ and $Ce(TMHD)_4$.

We determine firstly the stability of hydroxylated TiO_2 surfaces and reaction pathway and barrier calculations show that ligand elimination is favourable on anatase $TiO_2(001)$ and rutile $TiO_2(110)$ for the $Ce(MeCp)_3$ precursor, but is not favourable on a-$TiO_2(101)$ and r-$TiO_2(100)$. For $Ce(THMD)_4$, the ligand elimination on the majority surface facets of anatase and rutile TiO_2 are not favourable. The moderate cost for bond breaking of gas-phase $Ce(THMD)_4$, indicate that the deposition could proceed via chemical vapour deposition (CVD), rather than ALD.

The thermogravimetric studies indicated that $Ce(^iPrCp)_3$ is unstable and cannot be successfully delivered into the ALD reactor. However, $Ce(TMHD)_4$ was successfully delivered. The experimental attempts for deposition of CeO_x using $Ce(TMHD)_4$ using water or ozone enriched synthetic air as oxidizing agent were not successful. The experimental results, consistent with DFT calculations, suggest that ALD of CeO_x clusters on the surface of both anatase and rutile TiO_2 is unfavorable using $Ce(TMHD)_4$ as precursor. However, with a high energy anatase (001) facet, the first principles results indicate that deposition is more favourable. Thus, engineering the surface facet of TiO_2 in powders may be important to promote the deposition of Cerium-containing materials.

II. EXPERIMENTAL APPROACH

A. Computational Methods

All calculations are performed on the basis of spin-polarized DFT with the projector augmented wave (PAW) formalism[42], as implemented in the Vienna ab initio simulation package (VASP 5.4) code. The generalized gradient approximation (GGA) with the parameterization of Perdew-Burke-Ernzerhof (PBE) is used for the exchange-correlation functional.[43, 44] The valence electrons are 4 for Ti, 12 for Ce, 4 for C, 6 for O, 1 for H. The energy cutoff is set to be 400eV for the plane wave expansion. The convergence of energy and forces are set to be 1×10^{-4}eV and 0.01eV/□, respectively. The computed lattice constants for bulk anatase TiO_2 are a = b = 4.61□ and c= 2.96□ and they are a = b = 3.79□ and c = 9.58□ for bulk rutile TiO_2.

Four low-index TiO_2 surfaces are built using a slab model, including a-TiO_2(101), a-TiO_2(001), r-TiO_2(110) and r-TiO_2(100). For anatase TiO_2 nanoparticles, the majority surface is the lowest energy (101) facet, while the minority (001) surface is of interest as it is reactive and plays a key role in the catalytic reactivity.[4] For rutile TiO_2, (110) is the thermodynamically most stable facet. For bare TiO_2 and hydroxylated TiO_2, six trilayer slab models of TiO_2 are built with a (4×4) surfaces supercell. For the adsorption of metal precursor on stable hydroxylated TiO_2 surfaces, we have used a four tri-layer slab TiO_2 is built also in a (4×4) surface supercell. Due to the large supercell employed, Gamma-point sampling is used for these slab models.[45] The Hubbard U correction[46, 47] is applied to the partially filled Ti 3d and Ce 4f states. The U values are set to be 4.5eV for Ti and 5eV for Ce, which is consistent with our previous work.[48]

The surface energy of these surface facets is computed from

$$E_{surf} = \frac{1}{2A}\left(E_{total} - nE_{TiO2_{bulk}}\right) \quad (1)$$

Where A is the surface area of the supercell, n is the total number of TiO_2 units in the supercell, E_{total} and $E_{TiO2_{bulk}}$ are the total energy of the surface and the energy of a unit TiO_2 (anatase or rutile) in bulk.

The hydroxyl-terminations are studied with coverages ranging from 1/16 monolayer (ML) to 16/16ML on both anatase and rutile (100) surfaces, which each have 16 possible adsorption sites. On rutile (110), 1 ML has 8 sites. The Van der Waals correction is applied with PBE-D3 method.[49] The adsorption energy per hydroxylation group is calculated by

$$E_{ad} = (E_{total} - E_{slab} - n * E_{H2O)})/n \qquad (2)$$

where E_{total}, E_{slab}, and E_{H2O} are the energies of hydroxylated TiO_2, bare TiO_2 and free H_2O molecules, respectively. The activation barriers reported in this paper are computed using climbed image nudged elastic band (CI-NEB) method[50] with 6 images including the starting and ending geometries and with forces converged to 0.08eV/Å.

B. Experimental material and methods

Anatase and rutile TiO_2 nanoparticles (NPs) were purchased from Sigma-Aldrich. The specific surface area of these NPs were about 50 $m^2 \cdot g^{-1}$ and the particles size was <25 nm for anatase and <100 nm for rutile. Tris(i-propylcyclopentadienyl)cerium(III), $Ce(^iPrCp)_3$, and Tetrakis(2,2,6,6-tetramethyl-3,5-heptanedionato)cerium(IV), $Ce(TMHD)_4$, were purchased from Strem Chemicals.

1. Thermogravimetric Analysis

A Mettler Toledo TGA 2 - thermogravimetric analyser was used for studying the thermal behaviour of the investigated precursors and measuring their approximate sublimation temperature. Typically, about 10 mg of precursor was heated with a heating rate of 5 °C·min^{-1} in nitrogen flow, while its weight change was recorded. After obtaining the proper sublimation

temperature, a 240 min isothermal measurement was carried out aiming at studying the stability of precursor at the intended sublimation temperature.

2. Surface chemistry analysis

A Thermo Scientific™ K-Alpha™ X-ray photoelectron spectrometer, using monochromated aluminum Kα radiation with a photon energy of 1486.7 eV, was employed to study the surface chemistry of samples. The XPS data were acquired using an X-ray spot of 400 μm and a photoelectron energy step size of 0.1 eV for high resolution scans; while the differential charging was compensated using an electron flood gun. The obtained spectra were analysed using the CasaXPS software and the positions of peaks were calibrated using the aliphatic carbon 1s peak (284.8 eV).

3. Elemental analysis

The elemental composition of samples was studied using inductively coupled plasma – optical emission spectrometry (ICP-OES) method by means of a PerkinElmer Optima 5300 DV ICP-OES instrument. Approximately 25 mg of sample was digested in 4.5 ml 30% HCl+1.5 ml 65% HNO_3 + 0.2 ml 40% HF while microwave irradiation. The digestion time in the microwave was 60 min at maximum power. The digested samples were diluted to 50 ml with Milli-Q water prior to measurement.

4. Atomic layer deposition of cerium oxide

The pre-treatment of TiO_2 NPs and the atomic layer deposition (ALD) of cerium oxide (CeO_2) were carried out in a fluidized-bed atmospheric pressure ALD reactor already described elsewhere. [51, 52] Typically, 1.5 g of TiO_2 NPs was loaded in the reactor and after attaining the desired reaction temperature in the reaction bed, the NPs were pre-treated *in-situ* using ozone enriched synthetic air flow aiming at increasing the surface functional groups. The ozone enriched flow was obtained via flowing synthetic air through a Certizon Ozonizer C200 with

ozone output of 200 mg·min^{-1}. After ozone treatment, the sequential introduction of cerium precursor and oxidizing agent (ozone enriched synthetic air or water vapour containing nitrogen stream) was started with nitrogen purge intervals. The superficial gas velocity varied between 3.1 to 4.7 cm·s^{-1} during this process, depending on different steps of ALD cycle. The duration of the precursor and the oxidizing agent pulses was 3 min and the nitrogen purges was 2 min and the number of ALD cycles varied between 10 to 20.

III. DFT RESULTS

A. The nature and stability of hydroxylated anatase and rutile TiO_2 surfaces

Table 1. The calculated properties of low index TiO_2 surfaces. E_surf is the computed, relaxed surface energy.

	Surf. Area (nm^2)	E_surf (J/m^2)	No. of atoms	Neighbouring HO-H distance (Å)
a-TiO_2(101)	3.13	0.89	288	2.78
a-TiO_2(001)	2.30	1.05	288	1.90
r-TiO_2(110)	1.55	1.06	288	2.19
r-TiO_2(100)	2.19	1.17	288	2.02

Table 1 presents the computed properties of the TiO_2 surfaces used in this work. Since a (4×4) surface supercell is used to simulate the four surfaces, we have chosen 0.06ML (1/16ML), 0.50ML (8/16ML), 0.75ML (12/16ML), and 1ML terminations, with OH binding to surface Ti atoms and H binding to surface O atoms. On the r-TiO_2(110) surface, 8 OH and 8 H is 1ML coverage; for the other surfaces, 16 OH and 16 H is 1ML coverage. The surface area and

distance between neighbouring OH and H species are listed in Table 1. The calculated adsorption energies per hydroxyl group are listed in Table 2 and shown in Figure 1.

Table 2. The calculated adsorption energy, in eV, of water, per hydroxyl group, on anatase and rutile TiO_2 surfaces. The number of hydroxyl groups are listed in the parenthesis. On rutile (110), 1 ML has 8 sites; for the anatase and rutile (100) surfaces, 1ML has 16 sites.

	Adsorption energy /eV on anatase		Adsorption energy /eV on Rutile	
Coverage	a-TiO_2(101)	a-TiO_2(001)	r-TiO_2(110)	r-TiO_2(100)
0.06ML	-0.70 (1 OH)	-2.05 (1 OH)	-1.27 (1 OH)	-1.04 (1 OH)
0.50ML	-0.95 (8 OH)	-1.29 (8 OH)	-1.32 (4 OH)	-1.05 (8 OH
0.75ML	-1.01 (12 OH)	-0.97 (12 OH)	-1.29 (6 OH)	-1.08 (12 OH)
1.00ML	-0.86 (16 OH)	-0.98 (16 OH)	-0.37 (8 OH)	-1.06 (16 OH)

On the a-TiO_2(001) surface, the strongest water adsorption is at a coverage of 0.06ML and with increasing surface hydroxyl coverage, the adsorption energy per hydroxylation group decreases. It is however, still favourable to have up to 1 ML coverage of hydroxyls. At 1ML surface coverage, OH and H recombine into H_2O and desorb from surface, and the resulting surface hydroxyl coverage is reduced to 0.81ML (or 13/16ML). The repulsive effect between hydroxyl groups plays an important role in stabilizing the surface OH and H species.

However, this recombination is not observed on the other TiO_2 surfaces. With increasing surface coverage, the adsorption energies do not change significantly on a-TiO_2(101) and both rutile TiO_2 surfaces. The exception is for the highest coverage of 1ML on r-TiO_2(110) surface, which shows a weak adsorption energy of -0.37eV/ H_2O. This implies that the repulsive effect on the other TiO_2 surfaces is not that strong as on a-TiO_2(001) surface.

Table 1 shows that on the a-TiO_2(001) surface, the HO-H distance is the shortest (1.90□), which would indicate that the repulsive effect will be strongest on this surface and supports the results that at full hydroxyl coverage, the spontaneous surface recombination of OH and H species is promoted only on a-TiO_2(001) surface.

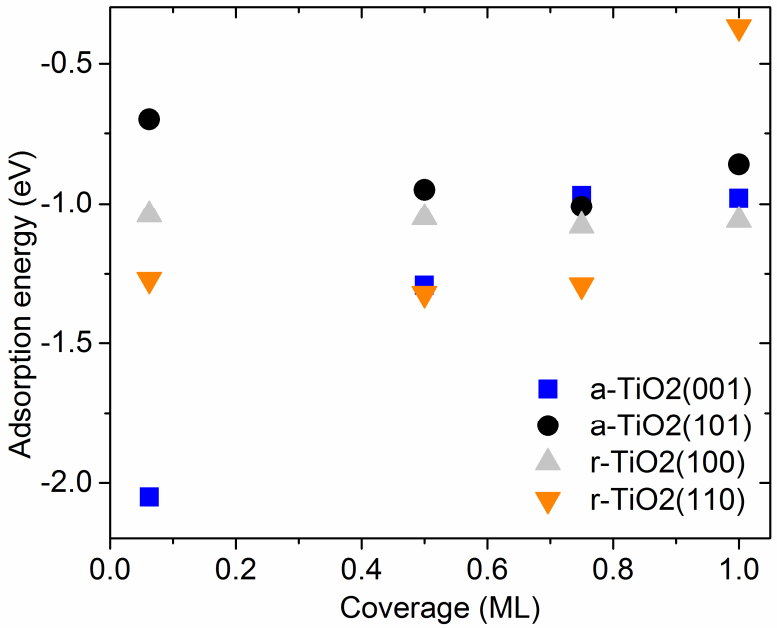

Fig. 1. The zero-K adsorption energy with different surface hydroxylation coverages on anatase and rutile TiO_2 surfaces.

To reveal the effect of temperature and pressure, we computed the Gibbs free energy of adsorption and the stability plots as a function of temperature at a pressure of 1 bar are shown in Figure 2. The Gibbs free energy is calculated from:

$$\Delta G(hydroxyl) = G_{(hydroxyl/TiO2)} - G_{TiO2} - G_{gas}(hydroxyl) \quad (3)$$

Here, we have ignored the changes in the vibration modes of the substrate. These contributions are usually much smaller than the total energy. Therefore, we can substitute the first two Gibbs energies with DFT-calculated total energies. The last term can be calculated by

$$G_{gas}(hydroxyl) = n * E_{H2O} + n * G_{H2O} + nk_B T ln^{(\frac{P}{P^0})} \quad (4)$$

The change in the Gibbs free energy is calculated by

$$\Delta G(nOH, nH) = E_{hydroxylation}^{(nOH,nH)} - E_{TiO2} - [n * E_{H2O} + n * G_{H2O} + nk_B T ln^{(\frac{P}{P^0})}] \quad (5)$$

where $E_{hydroxylation}^{(nOH,nH)}$ is the total energy of hydroxylated TiO_2 surfaces resulting from adsorption of n dissociated water molecules, E_{TiO2} and E_{H2O} are corresponding bare TiO_2 surfaces and free H_2O, respectively. G_{H2O} is the vibrational contribution to the free energy from the OH and H species in the gas phase at different temperatures with reference to H_2O. Experimentally, the temperature of the precursor and reactor in a typical ALD experiment are 180°C and 230°C. The operating pressure is 1 bar and this is used in the calculations.

On the a-TiO_2(001) surface, water formation during the relaxation means that the final stable coverage is 0.81ML we consider coverages of 0.06ML, 0.50ML, 0.75ML and 0.81ML. For the remaining TiO_2 surfaces, coverages of 0.06ML, 0.50ML, 0.75ML and 1ML are considered. From the computed Gibbs free energy at the temperature and pressure given above, the most stable surface hydroxylation coverages are 1ML on a-TiO_2(101), 0.81ML on a-TiO_2(001), 0.75 ML on r-TiO_2 (110) and 1 ML on r-TiO_2(100). The configurations of the most stable hydroxylated TiO_2 surfaces are shown in Figure 3. These hydroxyl coverages are then used to explore the adsorption and reaction of the cerium containing ligands in the next sections.

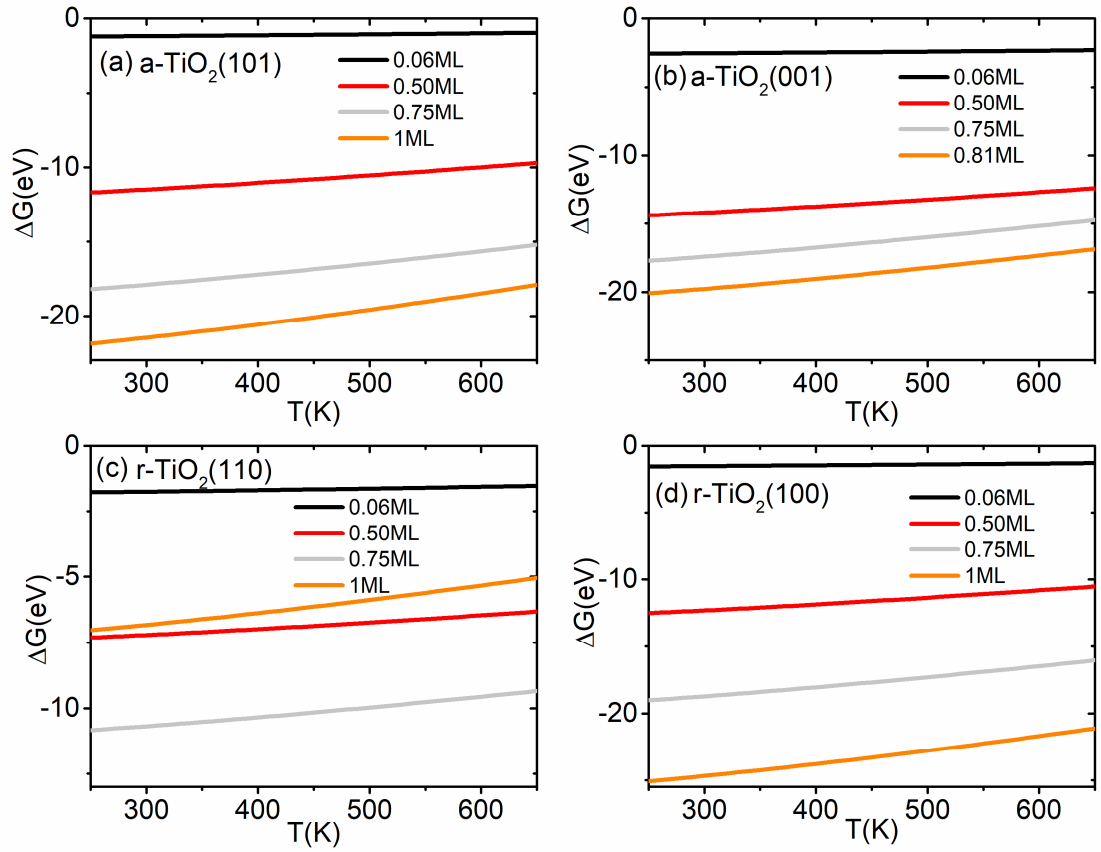

Fig. 2. Gibbs free energy (ΔG, in eV) of hydroxyl-terminated TiO_2 surfaces with respect to operating temperature. The pressure is set to be 1 bar.

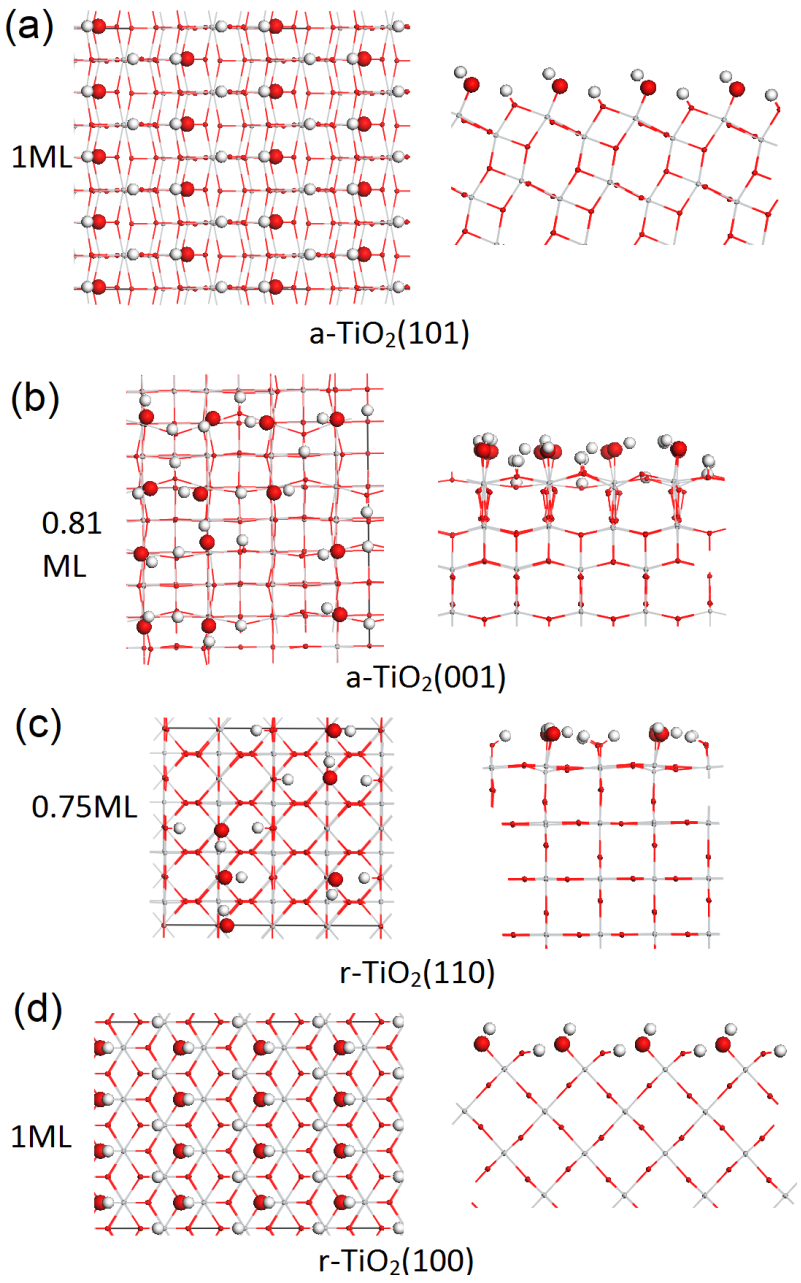

Fig. 3. The configurations of the most stable hydroxylation coverages on (a) a-TiO_2(101) surface, (b) a-TiO_2(001) surface, (c) r-TiO_2(110), and (d) r-TiO_2(100) surface. The Ti atoms and O atoms in the TiO_2 surfaces are represented by grey and red spheres and surface hydroxyl species H atom and O atom are represented by larger diameter white and red spheres, respectively.

B. Adsorption of metal precursors $Ce(TMHD)_4$ and $Ce(MeCp)_3$

The metal precursors $Ce(TMHD)_4$ and $Ce(MeCp)_3$ are adsorbed on the hydroxylated TiO_2 surfaces to investigate the precursor reaction mechanism. We use a four-layer TiO_2 substrate model instead of a six-layer TiO_2 substrate to reduce the computational cost. To check the effect of the TiO_2 slab thickness on our results, we have calculated the adsorption energies of metal precursor adsorbed on the two slab models and the computed differences are less than 10%, which is a reasonable difference for our discussion. The results of this comparison are presented in Table S1 in supporting information. Thus, a four-layer TiO_2 substrate model is used to study the metal precursor adsorption and reaction mechanism.

1. Structure of gas phase metal precursor $Ce(TMHD)_4$ and $Ce(MeCp)_3$

The gas-phase precursors of $Ce(TMHD)_4$ and $Ce(MeCp)_3$ are shown in Figure 4. $Ce(TMHD)_4$, with formula $Ce(C_{11}H_{19}O_2)_4$, has four ligands and each ligand contains 6 methyl groups. The Ce-O distances are in the range of 2.36Å to 2.46Å. $Ce(MeCp)_3$, with formula $Ce(C_6H_7)_3$, has three ligands and in each ligand, the carbon atoms in the Cp ring coordinate to Ce atom. The Ce-C distances are in the range of 2.77Å to 2.95Å. These longer distances reflect the different ionic radii of Ce^{4+} and Ce^{3+} cations in the precursors.

In the gas phase metal precursor, breaking of the bond between the Ce atom and the ligands is studied by removing one ligand (TMHD or MeCp) away from Ce atom. This process is endothermic for both precursors, with a moderate energy cost of 1.49eV for $Ce(TMHD)_4$ and higher cost of 3.60eV for $Ce(MeCp)_3$. For $Ce(TMHD)_4$, at elevated operating temperature, the precursor may dissociate and a chemical vapour deposition (CVD) process would dominate.

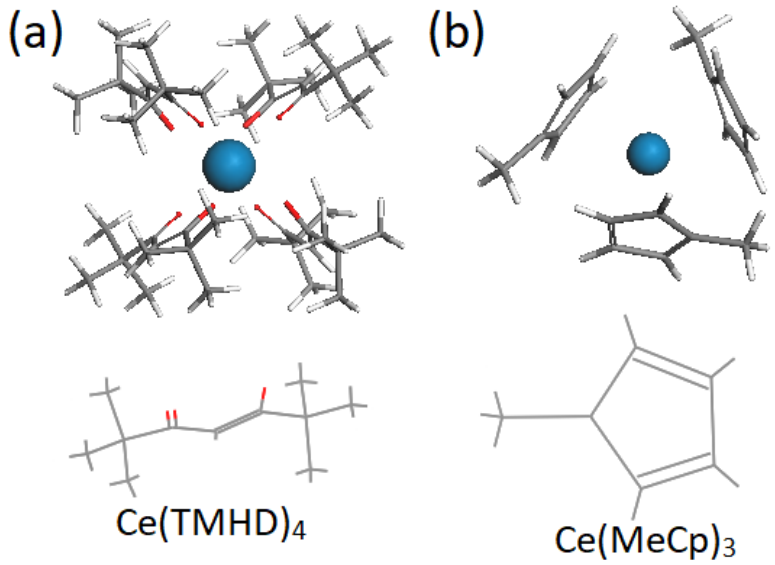

Fig. 4. The atomic structures of gas phase cerium precursors (a) $Ce(TMHD)_4$, and (b) $Ce(MeCp)_3$. The cerium, carbon, hydrogen and oxygen atoms are represented by blue, grey, white and red atoms.

2. *Adsorption of cerium precursors on hydroxylated anatase and rutile TiO_2 surfaces*

When adsorbed on hydroxylated TiO_2 surfaces, $Ce(TMHD)_4$ can take two different configurations. The **two-ligand** adsorption mode has two ligands oriented towards the surface and the other two ligands are oriented away from the surface and two ligands interact at the substrate. The **four-ligand** adsorption mode has the four ligands interacting at the surface. The preferred adsorption mode of the $Ce(MeCp)_3$ precursor has the three ligands interacting with the hydroxylated surfaces with the Ce atom in the centre of the precursor.

After the precursor is adsorbed the on hydroxylated TiO_2 surfaces and is allowed to relax, we find a strong rearrangement of the hydroxyl groups. If we remove the precursor and allow the resulting hydroxylated surface to relax, then there can be a new surface hydroxylation pattern that is more stable than the surface hydroxylation pattern described previously. The energy

changes after this precursor-induced rearrangement is listed in Table 3 are the change in energy compared to the original hydroxylated TiO_2 surfaces.

Table 3. The difference of the energy, ΔE^{OH} in eV, of hydroxylated TiO_2 surfaces before and after the precursor adsorption. This is the change in energy compared to the original hydroxylated TiO_2 surfaces.

		ΔE^{OH} in eV on anatase		ΔE^{OH} in eV on rutile	
		a-TiO_2(101)	a-TiO_2(001)	r-TiO_2(110)	r-TiO_2(100)
$Ce(TMHD)_4$	Two-ligand adsorption mode	-2.58	-0.14	-0.03	-0.01
$Ce(TMHD)_4$	Four-ligand adsorption mode	-2.74	-0.14	-0.04	-3.09
$Ce(MeCp)_3$		-2.72	-0.50	0.10	-1.35

For the $Ce(TMHD)_4$ precursor, the anatase (001) and rutile (110) surfaces are not strongly affected, while the energy change on a-TiO_2(101) and r-TiO_2(100) lie between -2.58 and -3.09 eV. The top view of these surfaces are shown in Figure 5. On a-TiO_2(101) surface, when we relax after removing the metal precursor, there is no water recombination. However, the distribution of hydroxyl species has changed, which corresponds to a symmetry breaking, and lowers the total energy of hydroxylated a-TiO_2(101).

On the r-TiO_2(100) surface, relaxation after removing the metal precursor 12 water molecules have been formed. This means that the, the final stable hydroxyl coverage is reduced to 0.25ML.

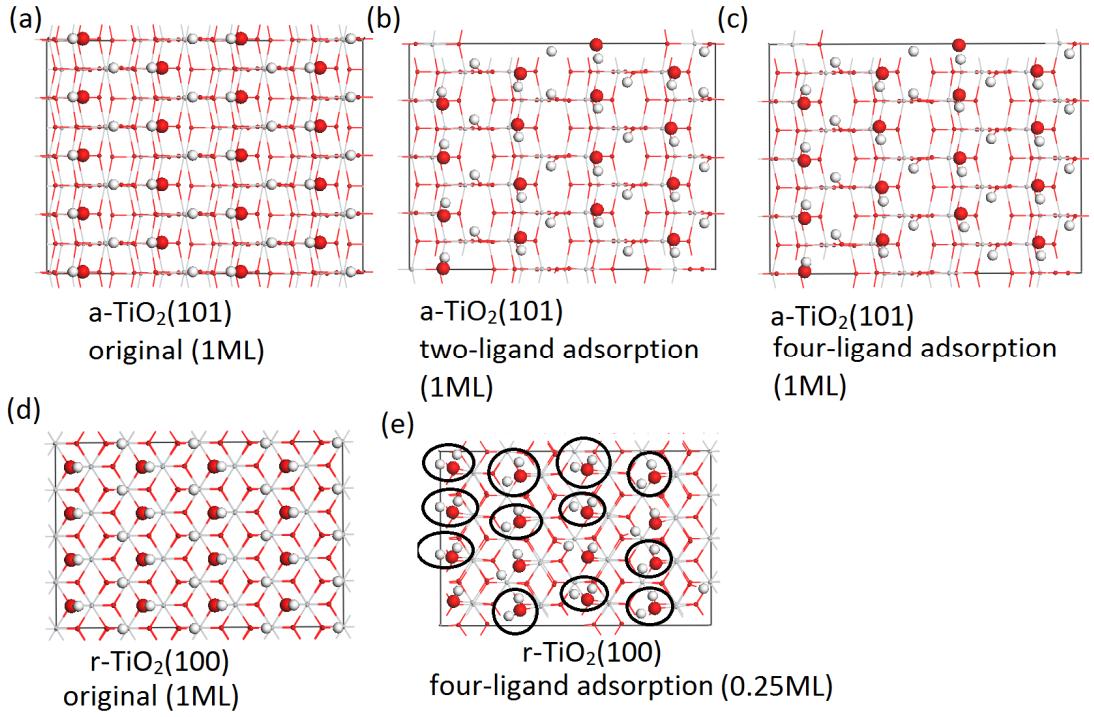

Fig. 5. The top view of a-TiO_2(101) with (a) original hydroxyl terminations, (b) hydroxyl terminations after two-ligand adsorption, and (c) hydroxyl terminations after four-ligand adsorption. (d) shows a top view of r-TiO_2(100) with the original hydroxyl terminations, and (e) hydroxyl terminations after four-ligand adsorption. The Ti atoms and O atoms in the TiO_2 surfaces are represented by grey and red spheres and surface hydroxyl species H atom and O atom are represented by larger diameter white and red spheres, respectively. The circles indicate the water formation after $Ce(THMD)_4$ adsorption.

Similarly, for $Ce(MeCp)_3$, significant differences in the total energy of hydroxylated surfaces are found on the a-TiO_2(101) and r-TiO_2(100) surfaces. The top view of these hydroxylated surfaces are shown in Figure 6. On a-TiO_2(101), the original hydroxyl groups show high symmetry. After removing the precursor from the surface, this symmetry has been broken, resulting in a lower energy, with the same coverage. On r-TiO_2(100) surface, after removing the precursor and relaxing, water forms and this reduces the stable hydroxyl coverage to 0.94ML.

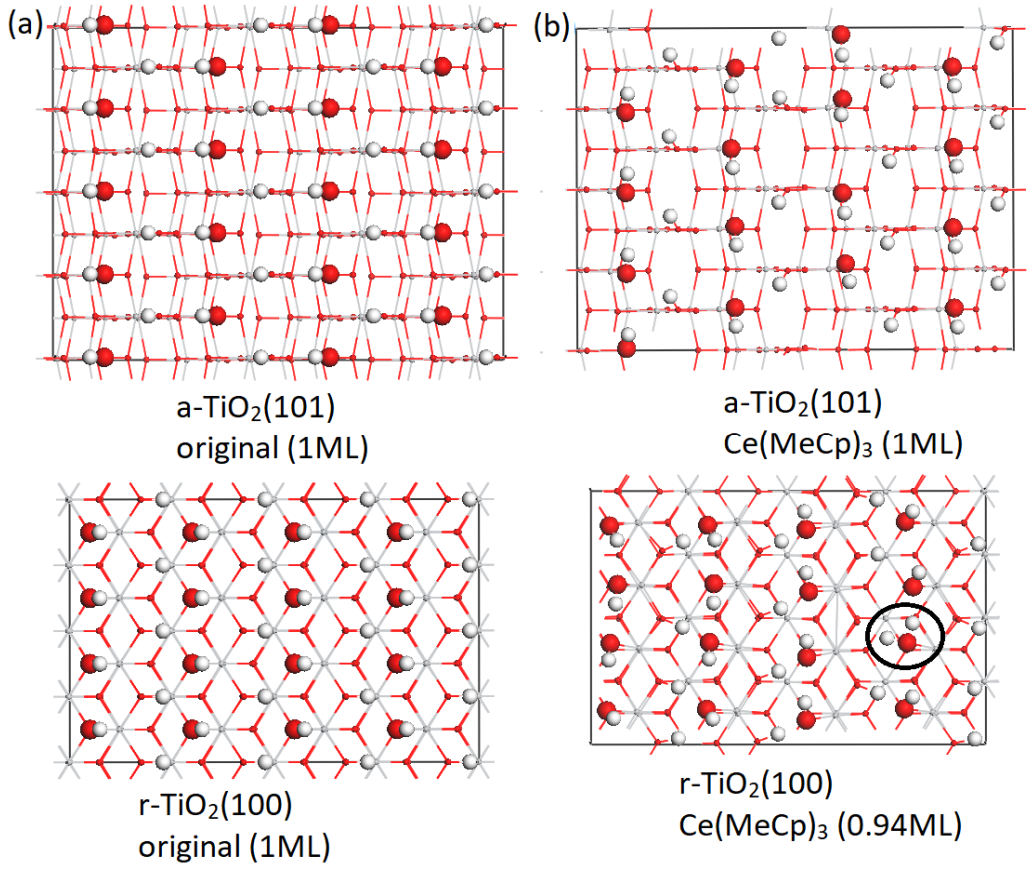

Fig. 6. The top view of a-TiO_2(101) with (a) original hydroxyl terminations and (b) hydroxyl terminations after $Ce(MeCp)_3$ adsorption, and top view of r-TiO_2(100) with (c) original hydroxyl terminations, and (d) hydroxyl terminations after $Ce(MeCp)_3$ adsorption. The Ti atoms and O atoms in the TiO_2 surfaces are represented by grey and red spheres and surface hydroxyl species H atom and O atom are represented by larger diameter white and red spheres, respectively. The circle indicates the water formation after $Ce(MeCp)_3$ adsorption.

With the above discussion in mind, we have therefore chosen the hydroxyl coverages that result from the above analysis and calculate the adsorption energy of the metal precursors with the formula:

$$E_{ad} = E[precursor/surface] - [E(precursor) + E(surface)] \quad (6)$$

$E(surface)$ is the total energy of the hydroxylated surface obtained after removing the precursor from the surface and relaxing. The results are summarized in Table 4.

Table 4. The calculated adsorption energies, ΔE^{ads} in eV, of precursor $Ce(TMHD)_4$ and $Ce(MeCp)_3$ on hydroxylated TiO_2 surfaces. The stable coverages of surface hydroxyl groups after precursor adsorption are listed in the brackets.

		ΔE^{ads} / eV on Anatase		ΔE^{ads} / eV on Rutile	
		TiO_2(101)	TiO_2(001)	TiO_2(110)	TiO_2(100)
$Ce(TMHD)_4$	Two-ligand adsorption mode	-0.91 (1ML)	-1.07 (0.81ML)	-1.39 (0.75ML)	-1.13 (1ML)
$Ce(TMHD)_4$	Four-ligand adsorption mode	-0.79 (1ML)	-0.85 (0.81ML)	-1.31 (0.75ML)	-1.38 (0.25ML)
$Ce(MeCp)_3$		-1.57 (1ML)	-1.01 (0.81ML)	-0.90 (0.75ML)	-1.89 (0.94ML)

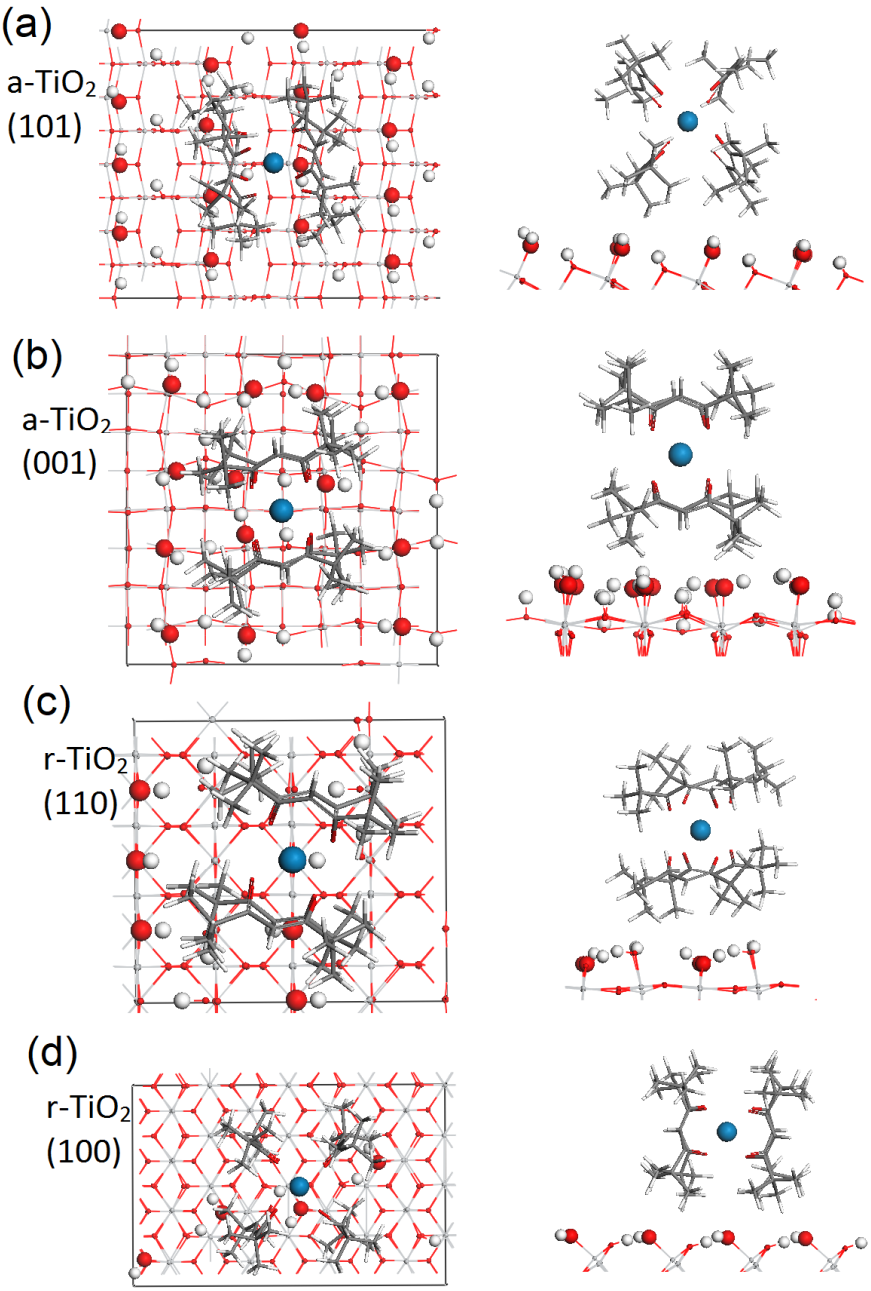

Fig. 7. The stable adsorption structures of $Ce(TMHD)_4$ adsorbed on hydroxylated (a) a-TiO_2(101) surface, (b) a-TiO_2(001) surface, (c) r-TiO_2(110) surface, and (d) r-TiO_2(100) surface. The Ti atoms and O atoms in the TiO_2 surfaces are represented by grey and red spheres and surface hydroxyl species H atom and O atom are represented by larger diameter white and red spheres, respectively. The cerium, carbon, and hydrogen atoms are represented by blue, grey, and white atoms.

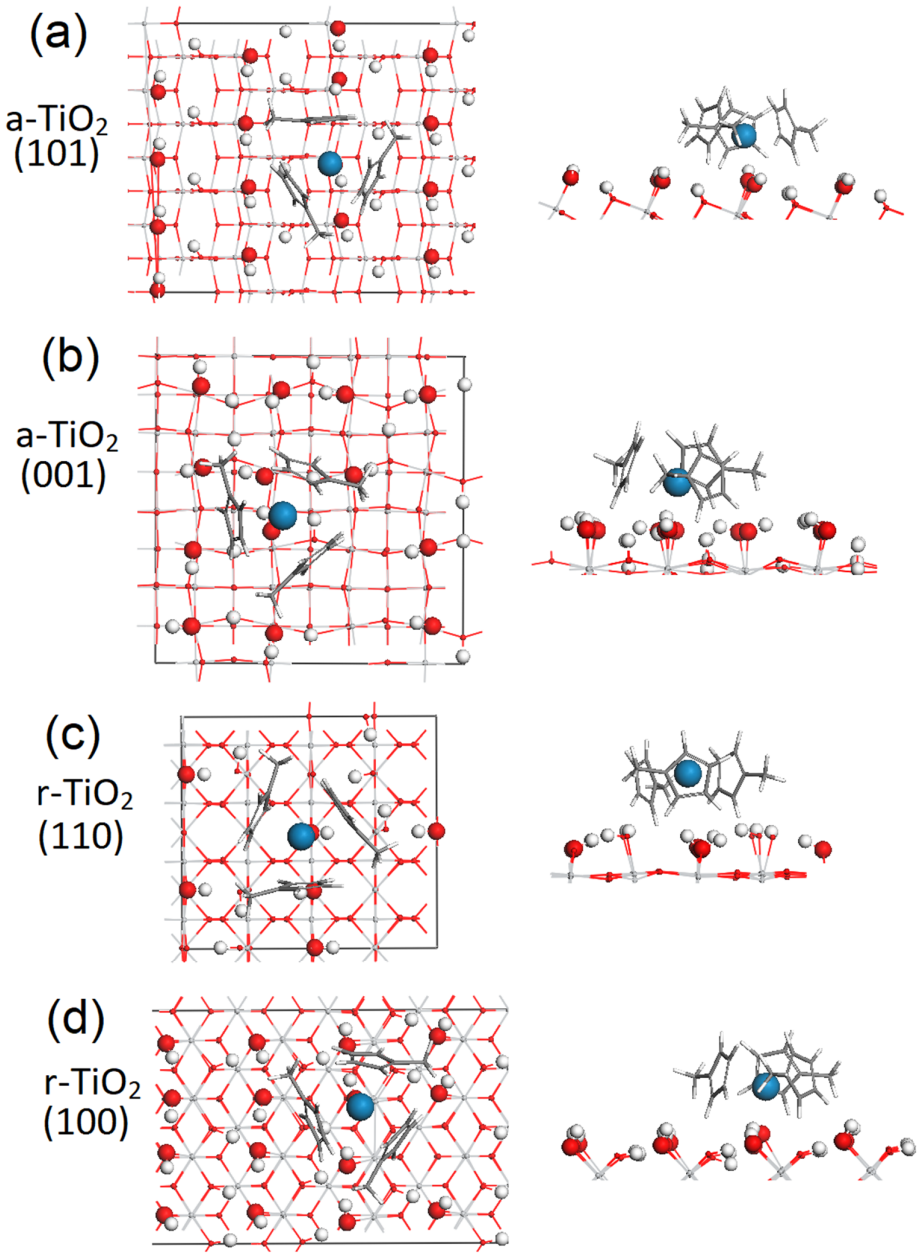

Fig. 8. The configurations of the most stable $Ce(MeCp)_3$ adsorbing on hydroxylated (a) a-TiO_2(101) surface, (b) a-TiO_2(001) surface, (c) r-TiO_2(110) surface, and (d) r-TiO_2(100) surface. The Ti atoms and O atoms in the TiO_2 surfaces are represented by grey and red spheres and surface hydroxyl species H atom and O atom are represented by larger diameter white and red spheres, respectively. The cerium, carbon, and hydrogen atoms are represented by blue, grey, and white atoms.

On the r-TiO_2(100) surface, with the lowest hydroxyl coverage, $Ce(TMHD)_4$ prefers four-ligand adsorption mode; while on the remaining surfaces, $Ce(TMHD)_4$ prefers the two-ligand adsorption mode, although the difference is at most 0.2 eV. The lower most stable adsorption modes appear to be at lower hydroxyl coverages. The configurations of the most stable $Ce(TMHD)_4$ precursor adsorbed on hydroxylated TiO_2 surfaces are shown in Figure 7. On the a-TiO_2(001) surface, the Ce-O distance are in the range of 2.34Å to 2.45Å; On a-TiO_2(101) surface, the Ce-O distance is 2.35Å to 2.44Å. On r-TiO_2(100) surface, the Ce-O distance is in the range of 2.35Å to 2.43Å; on r-TiO_2(110) surface, the Ce-O is in the range of 2.36Å to 2.45Å.

$Ce(MeCp)_3$ has the strongest adsorption strength on r-TiO_2(100), with an adsorption energy of -1.89 eV, with the weakest, but still appreciably strong, adsorption configuration on r-TiO_2(110). The most stable configurations of the precursor adsorbed on the hydroxylated TiO_2 surfaces are shown in Figure 8. After adsorbing on the TiO_2 surfaces and relaxing, the Ce-C distances are changed compared to the free molecule, where they are in the range of 2.77 Å to 2.95Å. On the a-TiO_2(001) surface, the Ce-C distance enlarges to between 2.82Å and 2.99Å. On the a-TiO_2(101) surface, the Ce-C distances are in the range of 2.70Å to 2.97Å. On the rutile surfaces, the Ce-C distance are in the range of 2.74Å to 2.98Å on r-TiO_2 (100) and 2.69Å to 2.91Å on r-TiO_2(110).

No spontaneous proton transfer is observed on both of the precursors after adsorbing on the surface. This implies that the ligand eliminations must overcome activation barriers.

3. *Reaction mechanism of precursor $Ce(THMD)_4$ on hydroxylated anatase and rutile TiO_2 surfaces*

The results of the first hydrogen transfer step and ligand desorption are shown in Figure 9 for anatase and Figure 10 for rutile TiO_2 surfaces. On the anatase TiO_2 surfaces, the precursor has a moderate adsorption strength, with computed adsorption energies of -1.07eV for a-TiO_2(001) and -0.91eV for a-TiO_2(101). On the a-TiO_2(001) surface, the proton transfer step is slightly exothermic with a gain of -0.13eV. However, the following bond breaking of Ce-$C_{11}H_{20}O_2$ has an energy cost of 1.09eV and the activation barrier would be at least 1.10 eV. This energy cost is slightly lower than bond breaking of gas phase Ce-THMD, which has an energy cost of 1.49eV. The loss of the first ligand to leave $Ce(THMD)_3$ on the surface is exothermic by *ca.* 0.60 eV.

Considering the a-TiO_2 (101) surface, there is a cost of 0.23 eV to protonate a THMD ligand but the loss of the ligand is overall endothermic, with an energy cost of 0.52 eV relative to the separated surface and precursor. The ligand elimination reaction via hydrogen transfer is not favoured on TiO_2(101) surface. Since this is the low energy surface facet of anatase and is therefore dominant in anatase films, this indicates that the $Ce(THMD)_4$ precursor may not be favourable for ALD of cerium materials on anatase TiO_2.

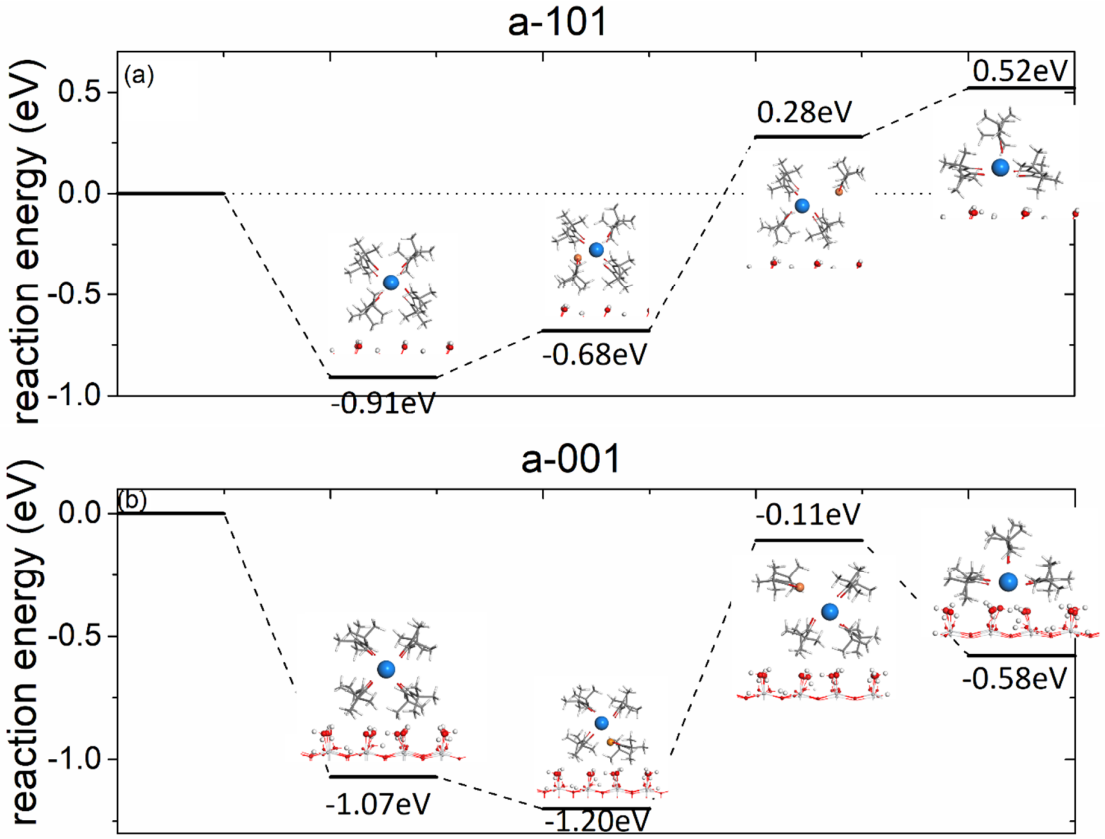

Fig. 9. The plotted reaction pathway of precursor $Ce(THMD)_4$ on hydroxylated anatase (a) $TiO_2(101)$ and (b) $TiO_2(001)$ surface. The Ti atoms and O atoms in the TiO_2 surfaces are represented by grey and red spheres and surface hydroxyl species H atom and O atom are represented by white and red spheres, respectively. The cerium, carbon, and hydrogen atoms are represented by blue, grey, and white atoms. For the hydrogen transfer, the transferred hydrogen atoms are represented by orange colour.

Turning now to the rutile TiO_2 surfaces, $Ce(THMD)_4$ has a moderate adsorption strength of -1.38eV on r-TiO_2(100) and -1.39eV on r-TiO_2(110). On the r-TiO_2(100) surface, Figure 10, the proton transfer is exothermic with a gain in energy of -0.22eV. The following bond breaking is endothermic and has an energy cost of 0.93eV for the release of the THMD ligand. On the r-TiO_2(110) surface, the proton transfer step and following bond breaking are endothermic.

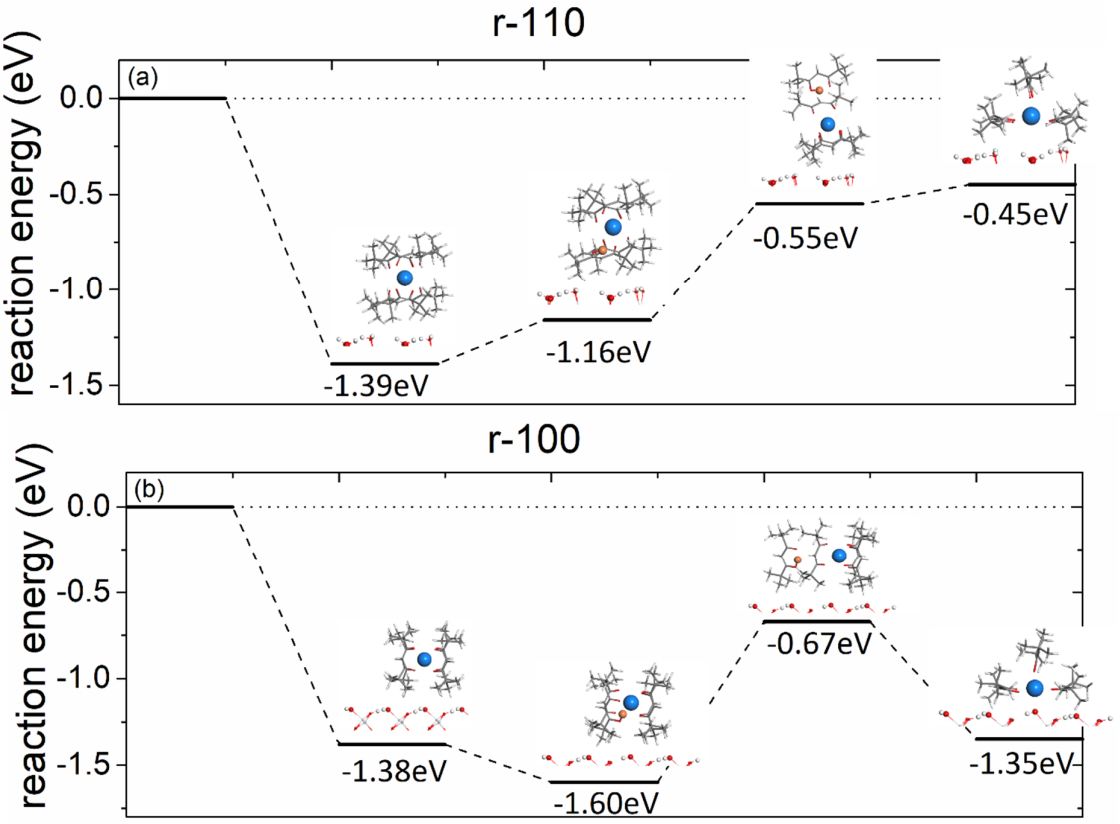

Fig. 10. The plotted reaction pathway of precursor $Ce(THMD)_4$ on hydroxylated rutile (a) $TiO_2(110)$ and (b) $TiO_2(100)$ surface. The Ti atoms and O atoms in the TiO_2 surfaces are represented by grey and red spheres and surface hydroxyl species H atom and O atom are represented by white and red spheres, respectively. The cerium, carbon, and hydrogen atoms are represented by blue, grey, and white atoms. For the hydrogen transfer, the transferred hydrogen atoms are represented by orange colour.

The results show that the ligand elimination process on the majority surface facets of anatase and rutile TiO_2 are endothermic and not favourable. It will therefore be difficult to deposit Ce atom onto hydroxylated TiO_2 surface using $Ce(TMHD)_4$ as precursor. In addition, the computed energy cost for direct Ce-ligand breaking is 1.49 eV. Due to the moderate cost for bond breaking of gas-phase $Ce(THMD)_4$, the deposition may instead proceed by chemical vapour deposition (CVD) at moderate temperatures, rather than by ALD.

4. Reaction mechanism of precursor $Ce(MeCp)_3$ on hydroxylated anatase and rutile TiO_2 surface

The MeCp ligand is eliminated by hydrogen transfer from surface hydroxyl and desorbs from surface as MeCpH. The plotted reaction pathways on anatase and rutile TiO_2 surfaces are shown in Figure 11 and Figure 12, respectively. On anatase TiO_2, the hydrogen transfers and CpH elimination steps are exothermic on a-TiO_2(001). However, the reaction is endothermic on the dominant a-TiO_2(101) facet.

On a-TiO_2(001) surface, the hydrogen transfer steps are exothermic by -0.55 eV for the first hydrogen transfer and -1.17eV for the second hydrogen transfer. However, the final hydrogen transfer and CpH release has a high energy cost and a high barrier of 1.07 eV, meaning that the most likely termination is CeMeCp. The computed activation barriers for the first two hydrogen transfer steps are moderate at 0.47eV and 0.44eV. If the three ligands are completely eliminated and the deposited Ce atom can bind to a square of surface oxygen atoms.

On the a-TiO_2(101) surface, the first hydrogen transfer and MeCpH elimination step is endothermic, while only the second hydrogen transfer step is exothermic. The first MeCp ligand elimination has a computed activation barrier of 2.88eV for hydrogen transfer, which is too high to permit this process at typical ALD temperatures. Due to the high barrier for the first hydrogen transfer step and the endothermic reaction energy, the remaining barriers are not calculated. The ligand elimination from $Ce(MeCp)_3$ is therefore difficult on this surface and we would expect Ce deposition on the a-TiO_2(101) surface to be unfavourable.

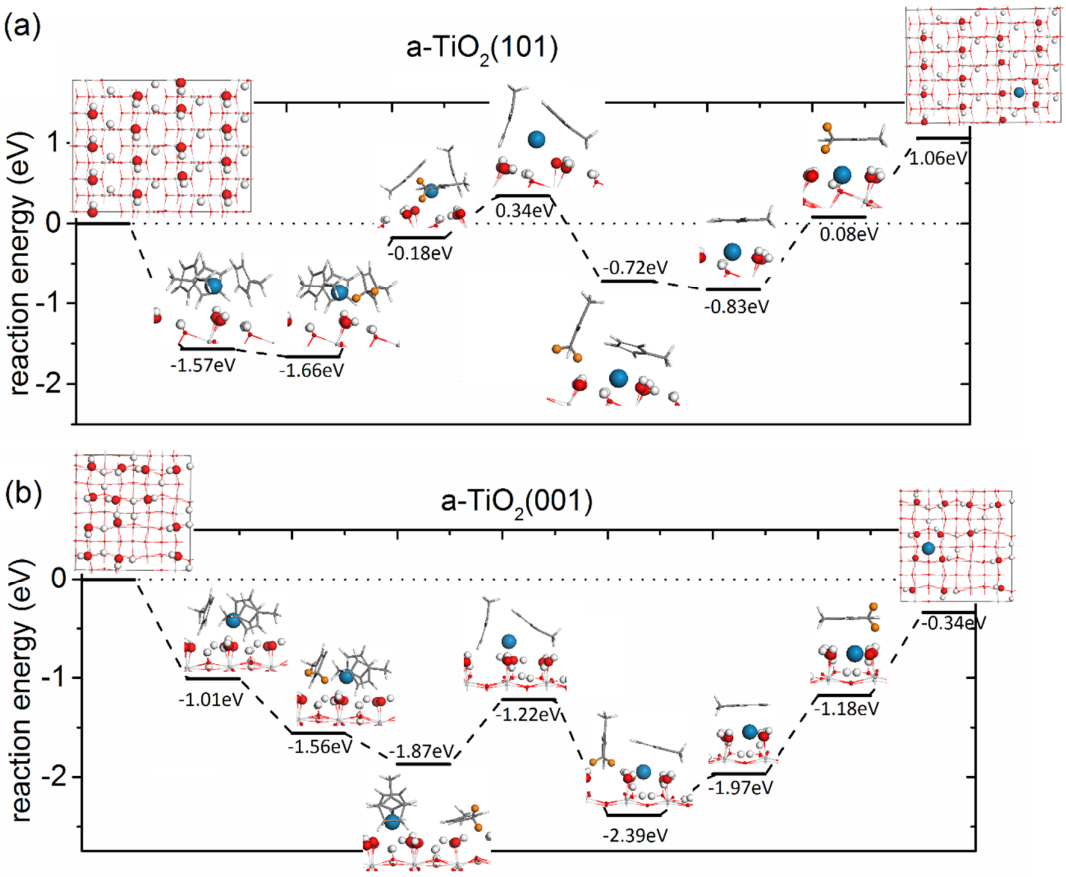

Fig. 11. The reaction pathway of the $Ce(MeCp)_3$ precursor on (a) a-TiO_2(101) surface and (b) a-TiO_2(001) surface. The Ti atoms and O atoms in the TiO_2 surfaces are represented by grey and red spheres and surface hydroxyl species H atom and O atom are represented by white and red spheres, respectively. The cerium, carbon, and hydrogen atoms are represented by blue, grey, and white atoms. For the hydrogen transfer, the transferred hydrogen atoms are represented by orange colour.

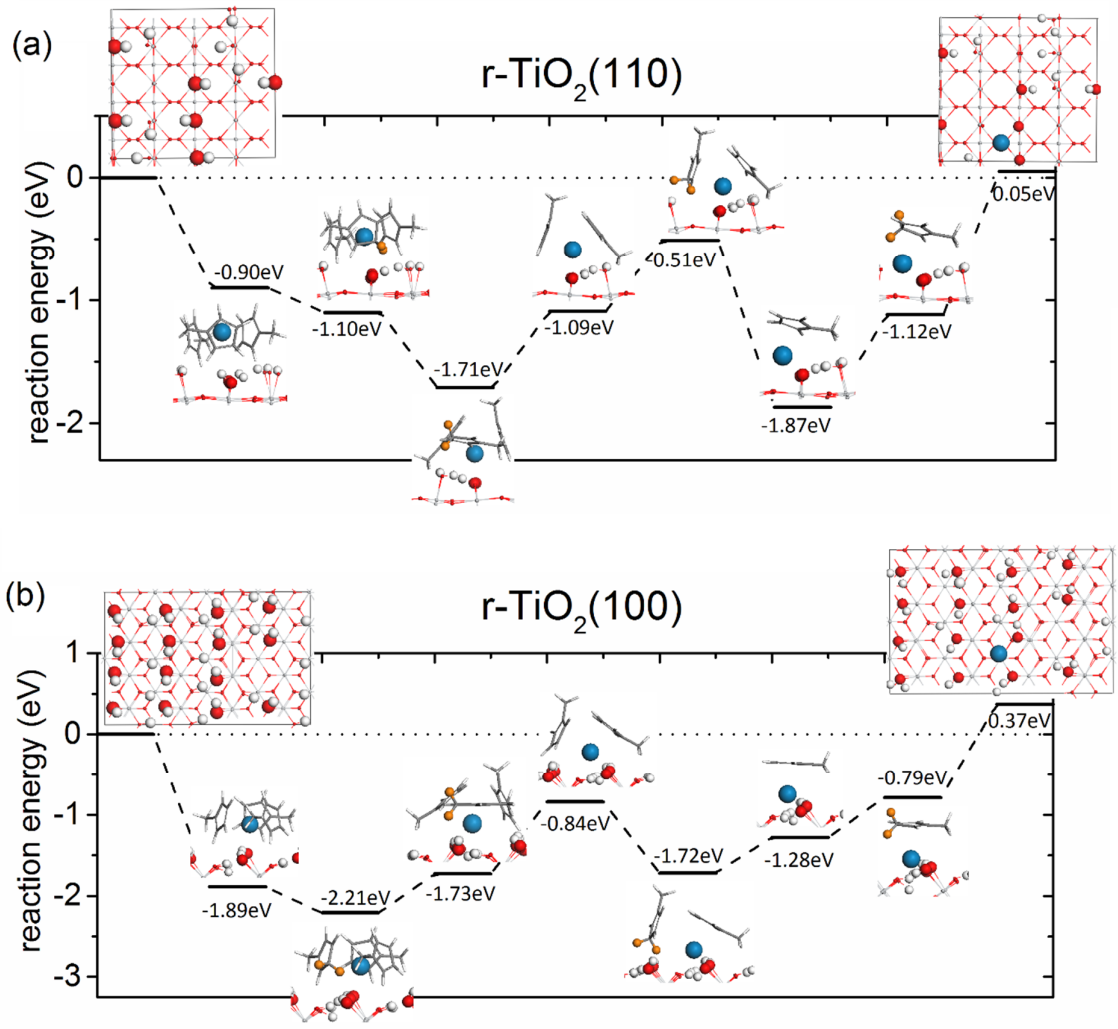

Fig. 12. The plotted reaction pathway of precursor $Ce(MeCp)_3$ on (a) r-TiO_2(110) surface and (b) r-TiO_2(100) surface. The Ti atoms and O atoms in the TiO_2 surfaces are represented by grey and red spheres and surface hydroxyl species H atom and O atom are represented by white and red spheres, respectively. The cerium, carbon, and hydrogen atoms are represented by blue, grey, and white atoms. For the hydrogen transfer, the transferred hydrogen atoms are represented by orange colour.

On the r-TiO_2(100) surface, the reactions for adsorption and elimination of two MeCpH ligands are overall exothermic, with computed activation barriers of 2.55 eV for the first hydrogen transfer step and 1.31 eV for the second hydrogen transfer step. The barrier for the third hydrogen transfer is not calculated. On r-TiO_2(100) surface, due to high barrier and endothermic reaction, there would be no Ce deposition.

On r-TiO_2(110) surface, the first hydrogen transfer step is exothermic with a computed activation barrier that is moderate with a value of 0.90eV. The second and third hydrogen transfers have computed activation barriers of 0.74eV and 1.31eV, respectively, although the energy cost for the third ligand elimination is high. Additionally, one H_2O molecule is formed on the surface.

To summarize, the ligand elimination reaction is potentially favourable on the a-TiO_2(001) while on the remaining surfaces, the preference will be for $Ce(MeCp)_3$ adsorption or elimination of up to two ligands. The structure of Ce deposited on a-TiO_2(001) is shown in Figure 13.

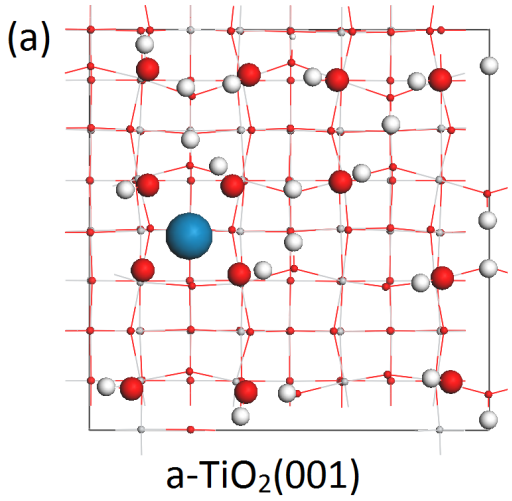

Fig. 13. The configurations of Ce atom deposited on the a-TiO_2(001) surface. The Ti atoms and O atoms in the TiO_2 surfaces are represented by grey and red spheres and surface hydroxyl species H atom and O atom are represented by larger diameter white and red spheres, respectively. The cerium is represented by blue atom.

IV. EXPERIMENTAL RESULTS

A. The optimum precursor sublimation temperature

Aiming at obtaining the optimum temperature for precursor sublimation and to investigate stability, thermogravimetric analysis (TGA) was carried out. Figure 14 depicts the TGA results of $Ce(^{i}PrCp)_3$ during heating up to 150 °C and an isothermal course of 70 °C. From the results in Figure 14(a), the sample starts losing weight at about 70 °C; this is obvious in first derivative of TGA (DTG) curve which manifests a peak at 72 °C. The increase of temperature results in further weight loss of $Ce(^{i}PrCp)_3$ which can be seen in form of several inflection points and peaks of DTG curve. The TGA results suggest 70 °C, the onset temperature of weight loss, as a reasonable sublimation temperature. The stability of $Ce(^{i}PrCp)_3$ at 70 °C was studied using isothermal TGA analysis; the temperature was increased to 70 °C with heating rate of 5 °C·min^{-1}, then this temperature was maintained for 240 min.

Figure 14(b) demonstrates that $Ce(^{i}PrCp)_3$ is unstable at 70 °C and it continuously loses weight. It is worth noting that the fresh $Ce(^{i}PrCp)_3$ is a dark blue solid; but the residue from the isothermal TGA was a brownish viscous liquid. The majority of the mass loss happens during the first 30 min of the isothermal course. This result demonstrates that $Ce(^{i}PrCp)_3$ is not sufficiently stable for ALD and is an unsuitable choice of precursor.

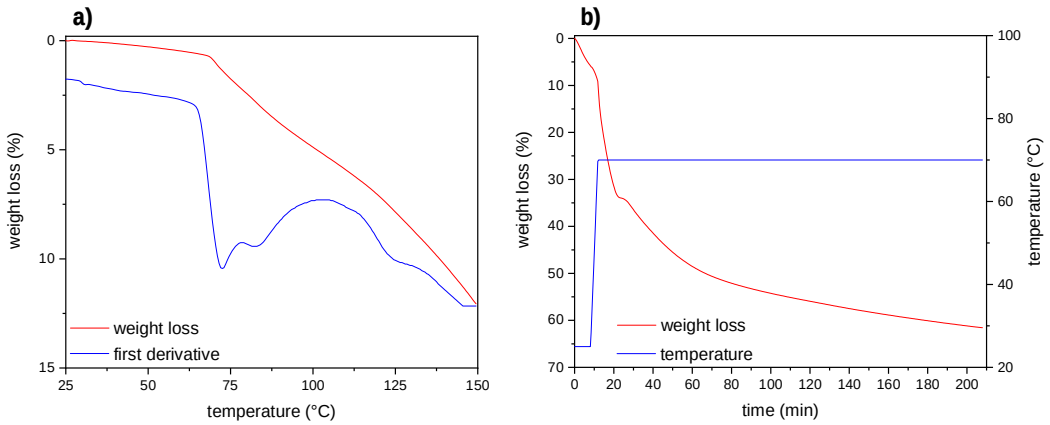

Figure 14. Thermogravimetric analysis of Ce(^{i}PrCp)$_3$ a) in temperature range of 25 – 150 °C and b) isothermal weight loss measurement at 70 °C.

A similar TGA study was conducted to investigate the thermal behaviour of Ce(TMHD)$_4$. The TGA curve of Ce(TMHD)$_4$, Figure 15-a reveals a weight loss onset at 180 °C corresponding to the sublimation temperature, which can be distinguished with a small peak in DTG curve at 188 °C. At temperatures above 220 °C, Ce(TMHD)$_4$ experiences rapid weight loss which can be attributed to the onset of decomposition. The DTG curve shows a prominent peak at 270 °C; this suggests that the majority of sample has decomposed at this temperature and this temperature should be avoided in ALD reactor to prevent the precursor decomposition. The isothermal TGA study of Ce(TMHD)$_4$ at 180 °C (Fig. 15-b) shows a steady weight loss of this material, indicating gentle sublimation of Ce(TMHD)$_4$. This demonstrates the stability of Ce(TMHD)$_4$ at this temperature and ease of precursor delivery to ALD reactor. The residue of this isothermal TGA study had the same appearance and colour of fresh Ce(TMHD)$_4$. According to TGA results, Ce(TMHD)$_4$ seems to be stable precursor that can be easily delivered to ALD reactor; hence, this precursor was selected for cerium ALD study.

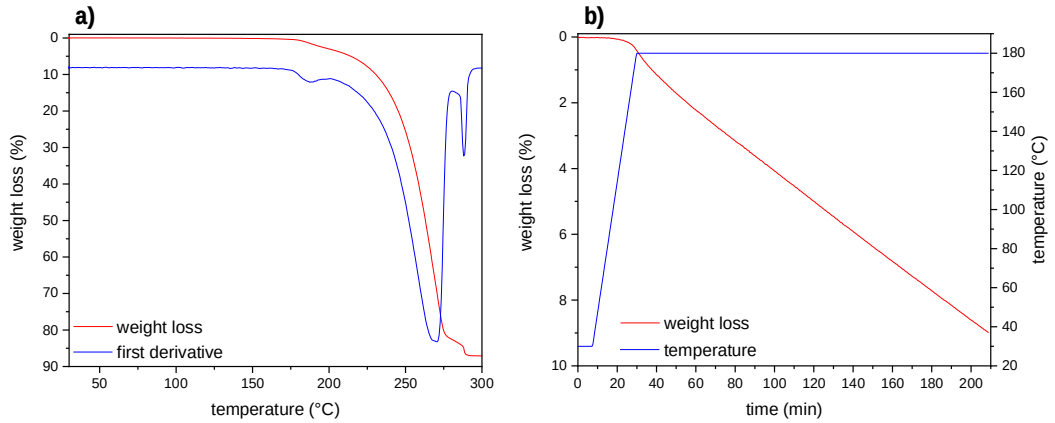

Figure 15. Thermogravimetric analysis of $Ce(TMHD)_4$ a) in temperature range of 25 – 300 °C and b) isothermal weight loss measurement at 180 °C.

To make sure that $Ce(TMHD)_4$ is stable at 180 °C and it is possible to deliver it intact into the ALD reactor, the XPS spectra of fresh $Ce(TMHD)_4$ was compared with the spectra of $Ce(TMHD)_4$ collected form the sublimator of the ALD setup after 20 hours of overall experiment at 180 °C, and the spectra of the $Ce(TMHD)_4$ condensate obtained from delivering the precursor into the ALD reactor at room temperature. The obtained spectra are presented in Figure 16.

The carbon 1s spectra of these three samples are identical which indicates the same type of organic ligands present in these samples. The oxygen 1s spectra of these samples also look similar in shape; however, there is subtle difference between the $Ce(TMHD)_4$ collected from sublimator and those two other samples. The deconvolution of oxygen 1s spectra of this sample reveals a tiny peak located at *ca*. 535.8 eV which is absent in two other spectra. This peak belongs to oxygen in silicon oxide [53] and probably is due to contamination of the sample with quartz wool which was used for packing the sublimator. The other difference between the oxygen 1s spectra of these three samples is the intensity of the peak located at ca. 529.2 eV which belongs to cerium-oxide bond [54, 55]. This peak has the highest intensity in the spectra of

$Ce(TMHD)_4$ condensate, collected from ALD reactor; the peak area percentage of peak at 529.2 eV in fresh, used, and condensate $Ce(TMHD)_4$ is 8.5 %, 11.8 %, and 16.3 %, respectively. This suggests that probably a portion of the TMHD ligands are detached and the oxygen-cerium bonds are formed in these samples. The high intensity of this peak in the condensate case also could be attributed to the method of sample preparation; the condensate $Ce(TMHD)_4$ was dissolved using ethanol and drop-casted on XPS sample holder that was heated up to 120 ℃ aiming at rapid evaporation of solvent. This process can easily result in cerium-oxygen bond formation in the sample. The cerium 3d spectra of these three samples reveals the same shape which is the typical shape spectra of cerium oxide [54, 55]. The XPS study of these three samples demonstrates that $Ce(TMHD)_4$ is successfully sublimated and delivered into the ALD reactor.

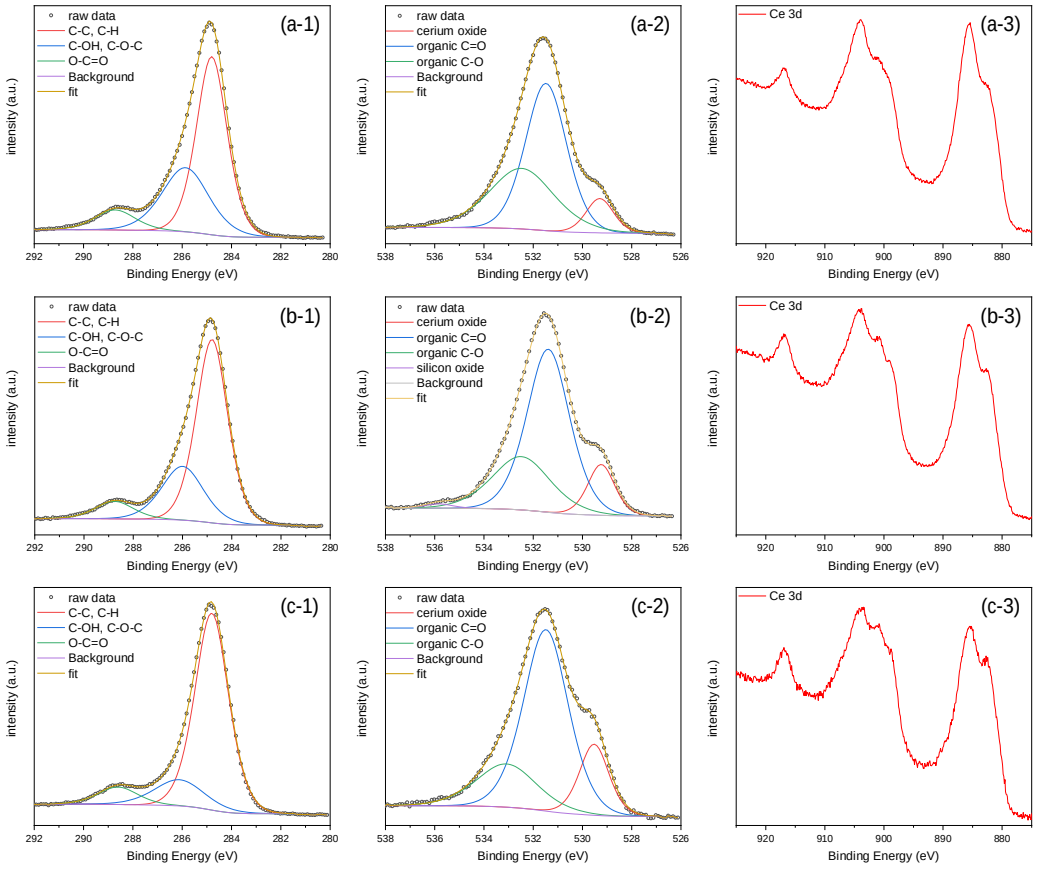

Figure 16. The XPS spectra of a) fresh $Ce(TMHD)_4$, b) used $Ce(TMHD)_4$, and c) $Ce(TMHD)_4$ condensate collected from ALD reactor: 1) carbon 1s, 2) oxygen 1s, and 3) cerium 3d spectra.

B. Atomic layer deposition of cerium oxide on titanium oxide nanoparticles

The first step of our attempts for ALD of cerium oxide on TiO_2 was pretreatment of TiO_2 using ozone enriched synthetic air, aiming at increasing the surface functional groups that can initiate/enhance the chemisorption of ALD precursor on the surface. Figure 17 depicts the XPS spectra of fresh and pretreated Anatase TiO_2. Both carbon 1s and oxygen 1s spectra demonstrate significant increase of the surface functional groups of TiO_2 after ozonation. The carbon 1s spectra of fresh TiO_2 reveals a main peak of aliphatic bonds, located at 284.8 eV. It also contains two minor peaks located at ca. 286.4 eV, corresponding to alcoholic/ether bonds, and ca. 288.6 eV attributed to ketone bonds. The carbon 1s spectra of fresh TiO_2 also contains a tiny peak at ca. 283.3 eV which is attributed to a carbon double bond which that is absent in the spectra of pretreated anatase. This peak probably is originated from carbon tape which is used for sample immobilization on sample holder.

The pretreatment of TiO_2 using ozone enriched synthetic air decreases the intensity of the aliphatic carbon peak and increases the intensity of the alcoholic/ether peak significantly. Also, a peak corresponding to carboxylic acid/ester components emerges in the pretreated sample [56, 57]. Table 5 summarizes the quantification of organic compounds calculated based on the peak area of different identified compounds (area %). This results demonstrate that the pretreatment of TiO_2 has significantly increased its surface functionality.

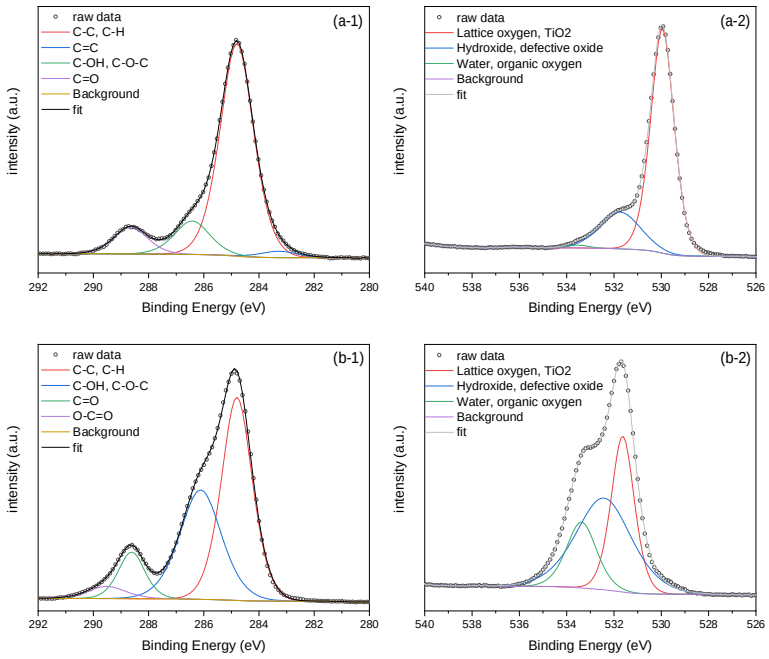

Figure 17. The XPS spectra of a) fresh anatase TiO_2 and b) pretreated anatase TiO_2: 1) carbon 1s and 2) oxygen 1s.

Table 5. The quantification (peak area %) of organic compounds calculated based on peak area of different identified compounds.

	XPS peak area percentage							
Sample	C-C / C-H	C=C	C-OH / C-O-C	C=O	O-C=O	Lattice oxygen	Hydroxide / defective oxide	Water / organic oxygen
Fresh a-TiO_2	75.26	2.49	12.56	9.69	n.a.	77.52	21.66	0.82
Pre-treated a-TiO_2	50.15	n.a.	36.30	9.84	3.7	33.83	47.66	18.51

Consistent with the results obtained for carbon 1s spectra, the oxygen 1s spectra indicated a significant change in pretreated TiO_2 after ozonation. The oxygen 1s spectra of fresh TiO_2

contains the main peak of lattice oxygen of TiO_2 at ca. 530 eV and a minor peak at ca. 531.7 eV that corresponds to surface hydroxides or defective oxides. There is also a tiny peak at *ca.* 533.5 eV which is attributed to surface water or organic oxygen. The oxygen 1s spectra of pre-treated TiO_2 reveals the same peaks, however, with significant difference between their ratios. As is shown in Figure 17, the majority of surface oxygen in this sample is in forms of hydroxide, defective oxide, organic oxygen, and water. The oxygen 1s spectra of pre-treated TiO_2 is shifted about 1 eV to higher binding energies which can be originated from increased defects on the surface of TiO_2 after ozonation [58]. Such increased surface functional groups and defects makes the pre-treated TiO_2 NPs a suitable support for any ALD process. Hence, the ozone treated TiO_2 NPs were used as support for attempts of cerium oxide ALD. However, the TiO_2 NPs without pre-treatment were also employed to investigate the effect of ozone treatment and ALD of cerium oxide.

Despite the abundance of surface functional groups after pretreatment of TiO_2 NPs, all the efforts for ALD of cerium oxide on both anatase and rutile TiO_2 NPs were unsuccessful. The temperature of the ALD reactor in these attempts was varied in the range of 200 – 260 °C and ozone or water were used as oxidizing agent. We avoided higher temperatures to work in what can be considered an appropriate temperature region and avoid the precursor decomposition which was observed at 270 °C using TGA study of $Ce(TMHD)_4$.

However, at the end of the process cerium oxide was not detectable using both elemental analysis methods employed in this work, i.e. XPS and ICP-OES. Figure 18 illustrates the XPS carbon 1s and cerium 3d spectra of rutile TiO_2 NPs pretreated using ozone enriched synthetic air after ALD attempts. The temperature of ALD reactor was 230 °C and ozone enriched synthetic air (Fig. 18-a) and water (Fig. 18-b) were used as oxidizing agent in these two cases. As obviously can be seen in Figure 18, ozonation has increased the surface functional groups of rutile TiO_2, as previously observed in the case of anatase TiO_2. However, the abundance of

such surface functional groups does not lead to $Ce(TMHD)_4$ activation and chemisorption on the surface of TiO_2 NPs. The cerium 3d spectra of these samples reveal noise/background and there is no peak detectable, demonstrating absence of cerium in these samples.

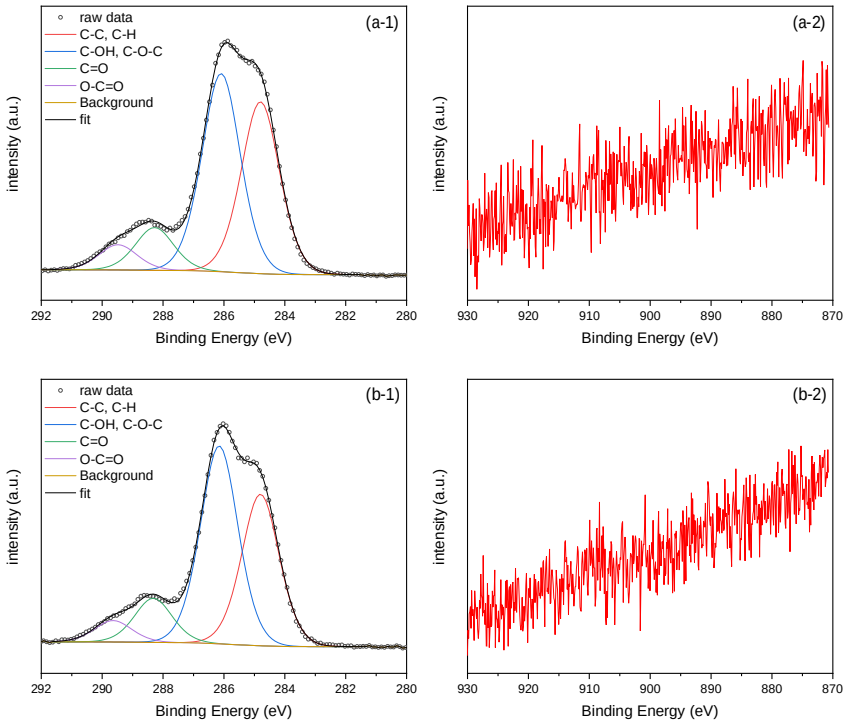

Fig. 18. The XPS spectra of Rutile TiO_2 pretreated using ozone enriched synthetic air after ALD attempts using a) ozone enriched synthetic air and b) water as oxidizing agent: 1) carbon 1s and 2) cerium 3d.

To make sure that the changes of the surface of TiO_2 NPs induced by ozonation does not hinder its surface reactivity, hence the cerium ALD, attempts were also done to deposit cerium oxide on the untreated TiO_2 NPs. Fig. 19 depicts the XPS spectra of anatase TiO_2 NPs that were used for ALD attempts without ozonation. The temperature of ALD reactor was 250 °C and ozone was used as oxidizing agent. The carbon 1s spectra of this sample again demonstrates the effect

of ozonation on surface functionality of TiO_2 NPs; as obviously can be seen, the majority of carbon in this sample is aliphatic carbon and a little amount of functional groups exist on the surface of this sample. There is also a relatively big carbon double bond peak that is originated from the carbon tape. Similar to previously discussed samples, there is no peak observable in the cerium 3d spectra of this sample that demonstrates ALD of cerium oxide on TiO_2 NPs is unlikely using the experimental condition of this work.

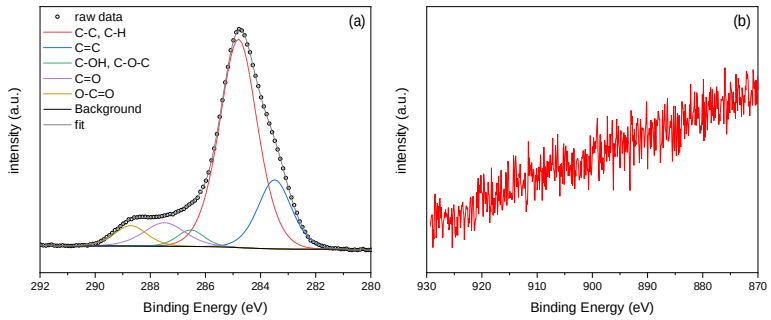

Fig. 19. The XPS spectra of Anatase TiO_2 without pretreatment after ALD attempts a) carbon 1s and b) cerium 3d.

Our observations suggest that there is a major energy barrier for activation of $Ce(TMHD)_4$ on the surface of TiO_2 that needs higher temperatures to surmount it and initiate the first step of ALD process, the chemisorption of $Ce(TMHD)_4$ on TiO_2. Hence, atomic layer deposition of cerium oxide on titanium oxide is not favorable in an appropriate temperature region that avoids decomposition of $Ce(TMHD)_4$.

V. DISCUSSION

Previous experimentally reported growth rates of CeO_x are generally quite low and in fact in this work we find no growth of CeO_x on TiO_2. For example, the thermal ALD using $Ce(THD)_4$ and O_3 has a low growth rate of 0.32 □/cycle. It is slightly increased to 0.43 □/cycle by modifying the ligand with phenanthroline using $Ce(THD)_3$phen and O_3.[24, 59] Additionally, the deposited CeO_x films have impurities including hydrogen, carbon, and fluorine. The cyclopentadienyl precursor $Ce(^iPrCp)_3$ also has a low growth rate of 0.2-0.3 □/cycle with H_2O as the co-reactant.[26, 60] If the O-source is changed to O_2 plasma, the deposited film is impurity-free but has a low growth rate of 0.35 □/cycle.[61] The growth rate is greatly improved to 1.9 □/cycle using a novel heteroleptic cyclopentadienyl-amidinate precursor $Ce(iPeCp)_2$(N-iPr-amd).[30] However, the synthesis of heteroleptic cerium complex is rather difficult.

TiO_2 is naturally present in three main phases including anatase, brookite, and rutile. Anatase is the most stable polymorph at the nanoscale. Two representative surface facets are a-TiO_2(001) and a-TiO_2(101). A-TiO_2(101) is the majority facet and a-TiO_2(001) is the minority facet but has high activity.[8] For rutile crystallites, r-TiO_2(110) surface is the thermodynamically most stable crystal face and the dominating facet. Here, the experimentally reported low deposition rate is explained by the non-favorable ligand elimination reaction on the majority facet a-TiO_2(101). Our DFT results and barrier analysis are in line with experimental results. The surface facet of TiO_2 plays an important role in precursor adsorption and reaction.

VI. CONCLUSION

The deposition of CeO_x onto TiO_2 surfaces is studied with density functional theory calculations. The nature and stability of surface hydroxyl groups on anatase and rutile TiO_2 surfaces are first investigated. The computed Gibbs free energy indicates that at operating condition (temperature 230°C, pressure 1 bar), the most stable surface hydroxylation coverages

are 0.81ML on a-TiO_2(001) surface, 1ML on a-TiO_2(101) and r-TiO_2(100) surfaces, and 0.75ML on r-TiO_2(110) surface. Two presentative Ce atom precursors, $Ce(TMHD)_4$ and $Ce(MeCp)_3$, are placed on these stable hydroxylated TiO_2 surfaces. For both precursors, upon adsorption, there is surface hydroxyl recombination and H_2O formation on r-TiO_2(100) surface and breaking of symmetry of hydroxyl groups on a-TiO_2(101) surface, which result in lower energy of hydroxylated TiO_2. The final stable surface hydroxylation coverages are 0.25ML for $Ce(TMHD)_4$ adsorption on r-TiO_2(100) surface and 0.94ML for $Ce(MeCp)_3$ adsorption on r-TiO_2(100) surface.

For gas-phase Ce metal precursor, the breaking of bond between Ce atom and ligand is endothermic. $Ce(TMHD)_4$ has a moderate energy gain of 1.49eV. The ligand elimination process starts with Ce-ligand bond breaking. The deposition using $Ce(TMHD)_4$ precursor is temperature sensitive. At elevated temperature, the deposition changes to chemical vapour deposition process. $Ce(MeCp)_3$ has a high energy gain of 3.60eV. The ligand elimination process is via hydrogen transfer from surface hydroxyl group. The computed barriers are moderate on a-TiO_2(001) and r-TiO_2(110) surfaces for all hydrogen transfer steps. The three MeCp ligands are eliminated completely and the deposited Ce atom binds to surface O atom. However, there is no Ce atom deposition on a-TiO_2(101) and r-TiO_2(100) surfaces due to endothermic reaction and high barriers. The computed barriers for the first hydrogen transfer are 2.88eV on a-TiO_2(101) and 2.55eV on r-TiO_2(110). The formation and desorption of MeCpH are not favoured. For TiO_2 nanoparticle, a-TiO_2(101) is the majority surface facet. The experimentally reported lack of CeO_x deposition can be explained by the non-favourable ligand elimination process on low energy surface facets of TiO_2.

ACKNOWLEDGMENTS

JI and MN acknowledge support from Science Foundation Ireland through the ERA.Net for Materials Research and Innovation (M-ERA.Net 2), Horizon 2020 grant agreement number 685451, SFI Grant Number SFI/16/M-ERA/3418 (RATOCAT) and the SFI-NSF China project, Grant Number SFI/17/NSFC/5239 (NITRALD). We acknowledge access to SFI funded computing resources at Tyndall Institute and the SFI/HEA funded Irish Centre for High End Computing. SS van JRvO acknowledge support from The Netherlands Organisation for Scientific Research, through the ERA.Net for Materials Research and Innovation (M-ERA.Net 2), Grant Number 732.017.101.

References

1. H. Tada, M. Fujishima and H. Kobayashi, Chem. Soc. Rev. **40**, 4232 (2011).
2. L. Li, J. Yan, T. Wang, Z.-J. Zhao, J. Zhang, J. Gong and N. Guan, Nat. Commun. **6**, 5881 (2015).
3. Z. Xing, J. Zhang, J. Cui, J. Yin, T. Zhao, J. Kuang, Z. Xiu, N. Wan and W. Zhou, Appl. Catal. B **225**, 452 (2018).
4. A. Vittadini, M. Casarin and A. Selloni, Theor. Chem. Acc. **117**, 663 (2007).
5. L.-M. Liu, P. Crawford and P. Hu, Prog. Surf. Sci. **84**, 155 (2009).
6. T. Fujino, M. Katayama, K. Inudzuka, T. Okuno, K. Oura and T. Hirao, Appl. Phys. Lett. **79**, 2716 (2001).
7. P. M. Kowalski, B. Meyer and D. Marx, Phys. Rev. B **79**, 115410 (2009).
8. X.-Q. Gong and A. Selloni, J. Phys. Chem. B **109**, 19560 (2005).
9. W. Xie, R. Li and Q. Xu, Sci. Rep. **8**, 8752 (2018).
10. R. Jaiswal, N. Patel, D. C. Kothari and A. Miotello, Appl. Catal. B **126**, 47 (2012).
11. L. H. Huang, C. Sun and Y. L. Liu, Appl. Surf. Sci. **253**, 7029 (2007).
12. L. A. Harris and A. A. Quong, Phys. Rev. Lett. **93** (8), 086105 (2004).
13. J. Graciani, J. J. Plata, J. F. Sanz, P. Liu and J. A. Rodriguez, J. Chem. Phys. **132** (10), 104703 (2010).
14. J. B. Park, J. Graciani, J. Evans, D. Stacchiola, S. D. Senanayake, L. Barrio, P. Liu, J. F. Sanz, J. Hrbek and J. A. Rodriguez, J. Am. Chem. Soc. **132**, 356 (2010).
15. L. Barrio, G. Zhou, I. Gonzalez, M. Estrella, J. Hanson, J. Rodriguez, R. Navarro and J. Fierro, Phys. Chem. Chem. Phys. **14**, 2192 (2012).

16. M. Nolan, ACS Appl. Mater. Inter. **4**, 5863 (2012).

17. M. Nolan, A. Iwaszuk and K. A. Gray, J. Phys. Chem. C **118**, 27890 (2014).

18. A. Iwaszuk and M. Nolan, J. Mater. Chem. A **1**, 6670 (2013).

19. C. Marichy, M. Bechelany and N. Pinna, Adv. Mater **24**, 1017 (2012).

20. Z. Li, J. Sheng, Y. Zhang, X. Li and Y. Xu, Appl. Catal. B **166-167**, 313 (2015).

21. B. Yuan, Y. Long, L. Wu, K. Liang, H. Wen, S. Luo, H. Huo, H. Yang and J. Ma, Catal. Sci. Technol. **6**, 6396 (2016).

22. X. D. Zhou, W. Huebner and H. U. Anderson, Chem. Mater. **15**, 378 (2003).

23. M. M. Natile, G. Boccaletti and A. Glisenti, Chem. Mater. **17**, 6272 (2005).

24. J. Päiväsaari, M. Putkonen and L. Niinistö, J. Mater. Chem. **12**, 1828 (2002).

25. B. J. O'Neill, D. H. K. Jackson, J. Lee, C. Canlas, P. C. Stair, C. L. Marshall, J. W. Elam, T. F. Kuech, J. A. Dumesic and G. W. Huber, ACS Catal. **5**, 1804 (2015).

26. W. J. Maeng, I.-K. Oh, W.-H. Kim, M.-K. Kim, C.-W. Lee, C. Lansalot-Matras, D. Thompson, S. Chu and H. Kim, Appl. Surf. Sci. **321**, 214 (2014).

27. P. J. King, M. Werner, P. R. Chalker, A. C. Jones, H. C. Aspinall, J. Basca, J. S. Wrench, K. Black, H. O. Davies and P. N. Heys, Thin Solid Films **519**, 4192 (2011).

28. L. Du, K. Wang, Y. Zhong, B. Liu, X. Liu and Y. Ding, J. Mater. Sci. **55**, 5378 (2020).

29. J. S. Wrench, K. Black, H. C. Aspinall, A. C. Jones, J. Bacsa, P. R. Chalker, P. J. King, M. Werner, H. O. Davies and P. N. Heys, Chem. Vap. Depos. **15**, 259 (2009).

30. M. Golalikhani, T. James, P. V. Buskirk, W. Noh, J. Lee, Z. Wang and J. F. Roeder, J. Vac. Sci. Technol. A **36**, 051502 (2018).

31. A. S. Sandupatla, K. Alexopoulos, M.-F. Reyniers and G. B. Marin, J. Phys. Chem. C **119**, 13050 (2015).

32. T. Weckman and K. Laasonen, Phys. Chem. Chem. Phys. **17**, 17322 (2015).

33. C. Guerra-Nuñez, M. Döbeli, J. Michler and I. Utke, Chem. Mater. **29**, 8690 (2017).

34. G. N. Fomengia, M. Nolan and S. D. Elliott, Phys. Chem. Chem. Phys. **20**, 22783 (2018).

35. S. D. Elliott and J. C. Greer, J. Mater. Chem. **14**, 3246 (2004).

36. Z. Hu and C. H. Turner, J. Phys. Chem. B **110**, 8337 (2006).

37. Z. Hu and C. H. Turner, J. Am. Chem. Soc. **129**, 3863 (2007).

38. M. Nolan and S. D. Elliott, Chem. Mater. **22**, 117 (2010).

39. L. Huang, B. Han, B. Han, A. Derecskei-Kovacs, M. Xiao, X. Lei, M. L. O'Neill, R. M. Pearlstein, H. Chandra and H. Cheng, J. Phys. Chem. C **117**, 19454 (2013).

40. J. H. Han, L. Nyns, A. Delabie, A. Franquet, S. Van Elshocht and C. Adelmann, Chem. Mater. **26**, 1404 (2014).

41. M. E. Dufond, M. W. Diouf, C. Badie, C. Laffon, P. Parent, D. Ferry, D. Grosso, J. C. S. Kools, S. D. Elliott and L. Santinacci, Chem. Mater. **32**, 1393 (2020).

42. G. Kresse and D. Joubert, Phys. Rev. B **59**, 1758 (1999).

43. J. P. Perdew, J. A. Chevary, S. H. Vosko, K. A. Jackson, M. R. Pederson, D. J. Singh and C. Fiolhais, Phys. Rev. B **46**, 6671 (1992).

44. J. P. Perdew, K. Burke and M. Ernzerhof, Phys. Rev. Lett. **77**, 3865 (1996).

45. H. J. Monkhorst and J. D. Pack, Phys. Rev. B **13**, 5188 (1976).

46. C. Loschen, J. Carrasco, K. M. Neyman and F. Illas, Phys. Rev. B **75**, 035115 (2007).

47. C. J. Calzado, N. C. Hernández and J. F. Sanz, Phys. Rev. B **77**, 045118 (2008).

48. S. Rhatigan and M. Nolan, J. Mater. Chem. A **6**, 9139 (2018).

49. Y. Maimaiti and S. D. Elliott, J. Phys. Chem. C **119**, 9375 (2015).

50. G. Henkelman, B. P. Uberuaga and H. Jónsson, J. Chem. Phys. **113**, 9901 (2000).

51. F. Grillo, D. La Zara, P. Mulder, M. T. Kreutzer and J. R. van Ommen, J. Phys. Chem. C **122**, 19981 (2018).

52. J. R. van Ommen and A. Goulas, Mater. Today Chem. **14**, 100183 (2019).

53. A. U. Alam, M. M. R. Howlader and M. J. Deen, ECS J. Solid. State. Sc. **2**, P515 (2013).

54. D. R. Mullins, S. H. Overbury and D. R. Huntley, Surf. Sci. **409**, 307 (1998).

55. A. E. Hughes, R. J. Taylor, B. R. W. Hinton and L. Wilson, Surf. Interface Anal **23**, 540 (1995).

56. A. Fujimoto, Y. Yamada, M. Koinuma and S. Sato, Anal. Chem. **88**, 6110 (2016).

57. N. Dwivedi, R. J. Yeo, N. Satyanarayana, S. Kundu, S. Tripathy and C. S. Bhatia, Sci. Rep. **5**, 7772 (2015).

58. M. J. Jackman, A. G. Thomas and C. Muryn, J. Phys. Chem. C **119**, 13682 (2015).

59. M. Coll, J. Gazquez, A. Palau, M. Varela, X. Obradors and T. Puig, Chem. Mater. **24**, 3732 (2012).

60. K. C. Neoh, G. D. Han, M. Kim, J. W. Kim, H. J. Choi, S. W. Park and J. H. Shim, Nanotechnology **27**, 185403 (2016).

61. M. Kouda, K. Ozawa, K. Kakushima, P. Ahmet, H. Iwai, Y. Urabe and T. Yasuda, Jpn. J. Appl. Phys. **50**, 10PA06 (2011).